Cellular and Molecular Life Sciences (2023) 80:53
https://doi.org/10.1007/s00018-023-04695-x

Cellular and Molecular Life Sciences

ORIGINAL ARTICLE

LYST deficiency impairs autophagic lysosome reformation in neurons and alters lysosome number and size

Jenny Serra-Vinardell[1] · Maxwell B. Sandler[1] · Raffaella De Pace[2] · Javier Manzella-Lapeira[3] · Antony Cougnoux[4] · Keyvan Keyvanfar[5] · Wendy J. Introne[1] · Joseph A. Brzostowski[3] · Michael E. Ward[6] · William A. Gahl[1,7] · Prashant Sharma[7] · May Christine V. Malicdan[1,7]

Received: 22 July 2022 / Revised: 11 December 2022 / Accepted: 8 January 2023 / Published online: 28 January 2023

Abstract

Chediak–Higashi syndrome (CHS) is a rare, autosomal recessive disorder caused by biallelic mutations in the lysosomal trafficking regulator (*LYST*) gene. Even though enlarged lysosomes and/or lysosome-related organelles (LROs) are the typical cellular hallmarks of CHS, they have not been investigated in human neuronal models. Moreover, how and why the loss of LYST function causes a lysosome phenotype in cells has not been elucidated. We report that the LYST-deficient human neuronal model exhibits lysosome depletion accompanied by hyperelongated tubules extruding from enlarged autolysosomes. These results have also been recapitulated in neurons differentiated from CHS patients' induced pluripotent stem cells (iPSCs), validating our model system. We propose that LYST ensures the correct fission/scission of the autolysosome tubules during autophagic lysosome reformation (ALR), a crucial process to restore the number of free lysosomes after autophagy. We further demonstrate that LYST is recruited to the lysosome membrane, likely to facilitate the fission of autolysosome tubules. Together, our results highlight the key role of LYST in maintaining lysosomal homeostasis following autophagy and suggest that ALR dysregulation is likely associated with the neurodegenerative CHS phenotype.

Keywords Autolysosomes · Protolysosomes · Autolysosome tubule · Lysosome fission · iPSC · Chediak–Higashi syndrome

Introduction

Lysosomes are degradative organellar hubs in which the turnover of endocytic and autophagic cargo occurs. Lysosomes frequently change their position, number, and size to maintain their homeostasis to meet the needs of a constantly changing intracellular environment. Autophagic lysosome reformation (ALR) is an evolutionarily conserved cellular process that instigates at the culmination of autophagy to restore the cellular pool of free lysosomes. During ALR, tubular structures composed of lysosomal membrane components bud off from autolysosomes followed by the scission

✉ Jenny Serra-Vinardell
jennyserravinardell@gmail.com

✉ Prashant Sharma
sharmap@nih.gov

1 Medical Genetics Branch, National Human Genome Research Institute, National Institutes of Health, Bethesda, MD 20892, USA

2 Neurosciences and Cellular and Structural Biology Division, Eunice Kennedy Shriver National Institute of Child Health and Human Development, National Institutes of Health, Bethesda, MD 20892, USA

3 Twinbrook Imaging Facility, Laboratory of Immunogenetics, National Institute of Allergy and Infectious Diseases, National Institutes of Health, Rockville, MD 20892, USA

4 Division of Translational Medicine, Eunice Kennedy Shriver National Institute of Child Health and Human Development, National Institutes of Health, Bethesda, MD 20892, USA

5 National Heart, Lung, and Blood Institute, Flow Cytometry Facility, National Institutes of Health, Bethesda, MD 20892, USA

6 National Institute of Neurological Disorders and Stroke, NIH, Bethesda, MD 20892, USA

7 Undiagnosed Diseases Program, National Human Genome Research Institute (NHGRI), National Institutes of Health (NIH), Common Fund, Office of the Director, NIH, Bethesda, MD 20892, USA

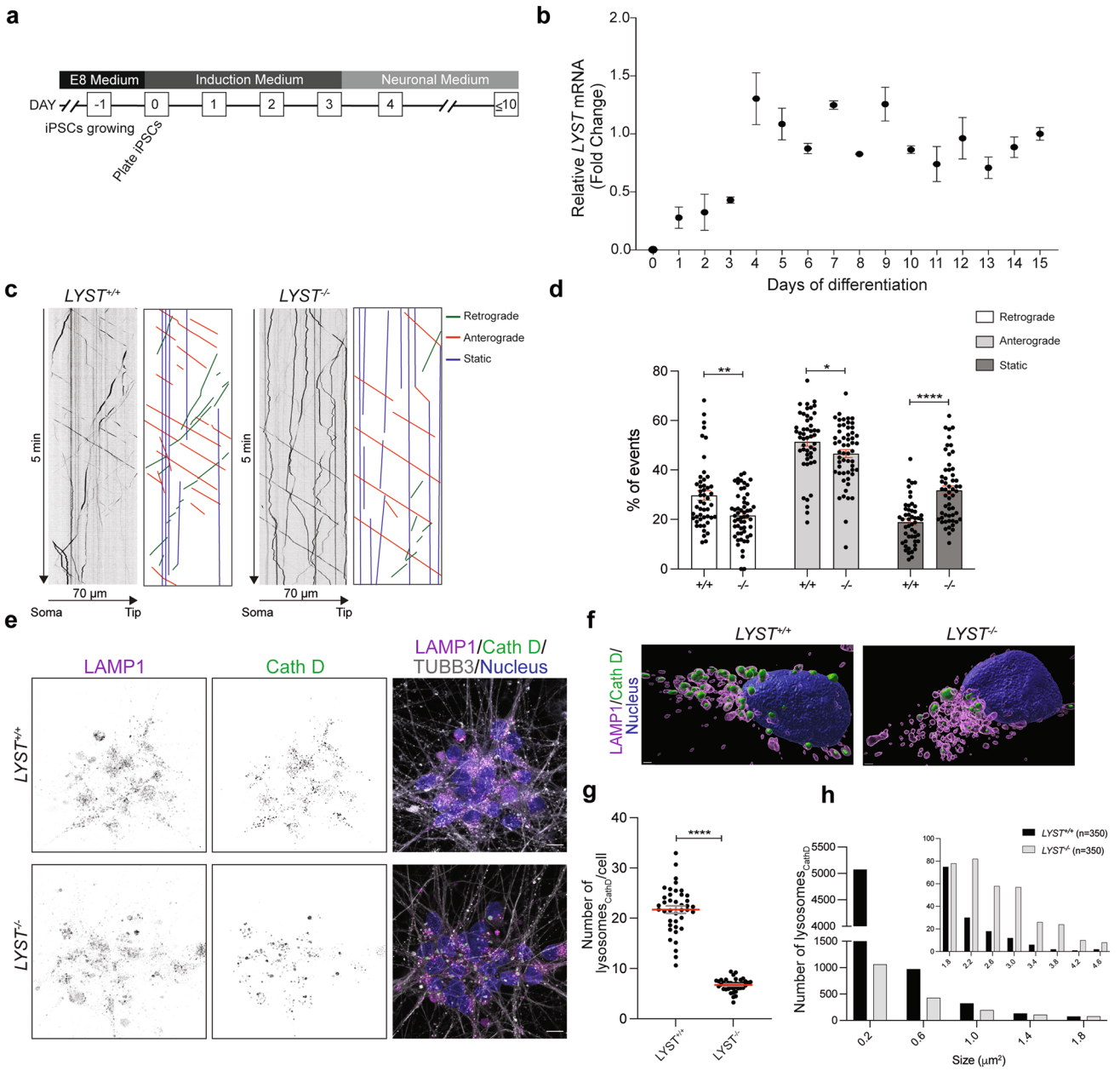

of small nascent lysosomes (protolysosomes) that ultimately mature and become functional lysosomes [1]. Precise regulation of lysosomal homeostasis is indispensable for terminally differentiated cells such as neurons. Consequently, the changes in the optimal lysosome functions are frequently associated with neurodegenerative diseases [2–4].

Chediak–Higashi syndrome (CHS) is a rare, autosomal recessive, lysosome-related organelle (LRO) disorder characterized by congenital partial oculocutaneous albinism, prolonged bleeding, immune dysregulation, and risk for development of hemophagocytic lymphohistiocytosis [5]. CHS patients also manifest developmental and degenerative neurological dysfunction [6]. The hallmark of the subcellular morphology associated with CHS is enlarged lysosomes and/or LROs, including melanosomes, lytic granules, Major Histocompatibility Complex class II compartments, and platelet-dense granules [7]; these organelles cluster near the perinuclear region of the cell.

CHS is caused by bi-allelic variants in the lysosomal trafficking regulator (*LYST*) gene [8, 9]. LYST and its murine orthologous *beige* (*Lyst*) are presumed to be regulators of lysosome and LRO size, either by acting as a negative regulator of lysosomal fusion events [10] or a positive regulator of lysosomal fission events [11, 12]. Moreover, as its name implies, the LYST protein may play a role in endolysosomal trafficking [13] and lysosome movement within the

◂**Fig. 1** LYST is not essential for the axonal transport of lysosomes but controls the number and the size of the perinuclear lysosomes. **a** Scheme describing a two-step (neuronal induction and maturation) protocol of i^{3}Neuron differentiation. **b** Fold changes in the levels of *LYST* mRNA over the 15 days of iPSCs (i^{3}N iPSC line) differentiation into i^{3}Neurons. **c** Representative kymographs of *LYST*$^{+/+}$ and *LYST*$^{-/-}$ i^{3}Neurons expressing LAMP1-mNeonGreen. The height of the kymographs represents acquisition time (5 min), while the width represents the length (70 µm) of the axon imaged. The corresponding diagram on the right side of each kymograph shows lines with positive or negative slopes. Lines in green and red represent retrograde and anterograde movements respectively, while vertical lines in blue depict static movements. **d** Quantification of the number of retrograde, anterograde, and static LAMP1-mNeonGreen particles in the mid-axon of *LYST*$^{+/+}$ and *LYST*$^{-/-}$ i^{3}Neurons. The number of moving and static particles is expressed as a percentage of the total number of events in each kymograph. Values are the mean ± SEM (in red) with dots representing individual axons from *LYST*$^{+/+}$ ($n=49$) and *LYST*$^{-/-}$ ($n=55$) i^{3}Neurons from two independent experiments. *$P<0.05$, **$P<0.01$, ****$P<0.0001$, unpaired two-tailed Mann–Whitney test. **e** Representative images of *LYST*$^{+/+}$ and *LYST*$^{-/-}$ i^{3}Neurons showing indirect immunofluorescence of LAMP1 (purple) and a luminal lysosomal protease cathepsin D (Cath D; green). The grey color represents ß-tubulin III (TUBB3), and the cell nuclei were visualized using Hoechst 33342 (in blue). Single-LAMP1 and Cath D channel images are shown in inverted greyscale. Scale bar 10 µm. See also Fig. S2a. **f** Three-dimensional surface reconstruction from an Airyscan z-stack image of the indirect immunofluorescence of LAMP1 (purple), Cath D (green), and Hoechst 33342 (blue; nucleus) of *LYST*$^{+/+}$ and *LYST*$^{-/-}$ i^{3}Neurons. Scale bar 1 µm. **g** Quantification of lysosome$_{CathD}$ per cell presented as mean (in red) ± SEM with dots representing the average of lysosome$_{CathD}$/cell per image analyzed. A total of 40 images from four independent experiments were analyzed that represent a total of 790 cells in both genotypes. ****$P<0.0001$, unpaired two-tailed Mann–Whitney test. See also Fig. S2b. **h** Histogram for lysosomes$_{CathD}$ size (area) distribution pooled from 350 cells from both, *LYST*$^{+/+}$ and *LYST*$^{-/-}$ i^{3}Neurons. The bin width is 0.4 µm^2. The distribution of sizes is presented in two separate histograms; the histogram shows the lysosomes$_{CathD}$ number up to 2.0 µm^2 area, and the histogram in the inset shows the distribution lysosomes$_{CathD}$ with the larger area, ranging between 1.6 to 4.8 µm^2. See also Fig. S2c

cell [11]. Mice carrying a homozygous missense variant (*Lyst*$^{lng3618/lng3618}$) showed giant lysosomes in the central and peripheral nervous systems that increase during aging and exhibit progressive degeneration accompanied by loss of Purkinje cells [14]. Later, it has been reported that the genetic background of *Lyst*-mutant mice dictates the severity of the neurodegenerative phenotype [15, 16]. However, the effect of LYST deficiency has not been studied in human neurons. Additionally, the large size of the LYST protein, 429 kilodaltons (kDa) [11], constitutes a significant barrier to manipulating its levels in attempts to precisely dissect its functional role in cells.

In this study, we define the role of LYST in neuronal lysosomes by establishing the first LYST-deficient human neuronal cell model from induced pluripotent stem cells (iPSCs) using CRISPR-Cas9 technology. We employed super-resolution fluorescence microscopy to demonstrate that LYST regulates lysosome number and size. Although LYST depletion does not interfere with autolysosome degradation capability, we observed a defective scission of the autolysosome tubules, which results in defective ALR. We also recapitulated this phenotype in neurons differentiated from CHS patients' iPSCs. To further explore the LYST function, we expressed LYST in neurons and U2OS cells using the piggyBac transposon system and found a significant increase in the number of small lysosomes. We revealed that LYST is highly recruited to LAMP1-positive organelles likely to facilitate the fission of the autolysosome tubules. Here, we conclude that LYST plays an important role in maintaining lysosomal homeostasis by regulating protolysosome scission during ALR.

Results

Generation of LYST-deficient neuronal cell model

To understand the role of LYST in neuronal lysosomes, we differentiated human iPSCs (i^{3}N iPSC line) into a uniform population of glutamatergic neurons using a doxycycline-inducible system [17, 18] (Fig. 1a). *LYST* expression was undetectable in undifferentiated iPSCs, suggesting that *LYST* is either not or expressed at a very low level in iPSCs. The addition of doxycycline induced the differentiation of iPSCs into cortical glutamatergic neurons (i^{3}Neurons) coincided with the detectable *LYST* expression that peaked on day four and remained mainly unchanged during differentiation (Fig. 1b). Using CRISPR-Cas9, we knocked out (KO) *LYST* in iPSCs and generated a clonal population of *LYST* KO (*LYST*$^{-/-}$) iPSCs (Figs. S1a and S1b). We confirmed and characterized the pluripotency and the genomic integrity of these iPSCs (Figs. S1c and S1d). Upon doxycycline induction, *LYST*$^{-/-}$ iPSCs were able to differentiate into glutamatergic neurons (Fig. S1e), and as expected, no *LYST* expression was detected in LYST-deficient (*LYST*$^{-/-}$) i^{3}Neurons (Fig. S1f).

LYST is dispensable for the axonal transport of lysosomes in neuronal cells

In neurons, lysosomes are distributed in axons, dendrites, and soma. The microtubule-dependent motor proteins mediate the movement of lysosomes. While some lysosomes are relatively static, others move bidirectionally along microtubule tracks between plus-ends (anterograde, towards axons) and minus-ends (retrograde, towards the soma). To explore the lysosome axonal transport in LYST deficient neurons, we transduced *LYST*$^{+/+}$ and *LYST*$^{-/-}$ i^{3}Neurons with a lysosome-associate membrane protein-1 (LAMP1) fused with a fluorescent protein mNeonGreen. We then performed time-lapse imaging in the mid-axon to follow lysosome movement

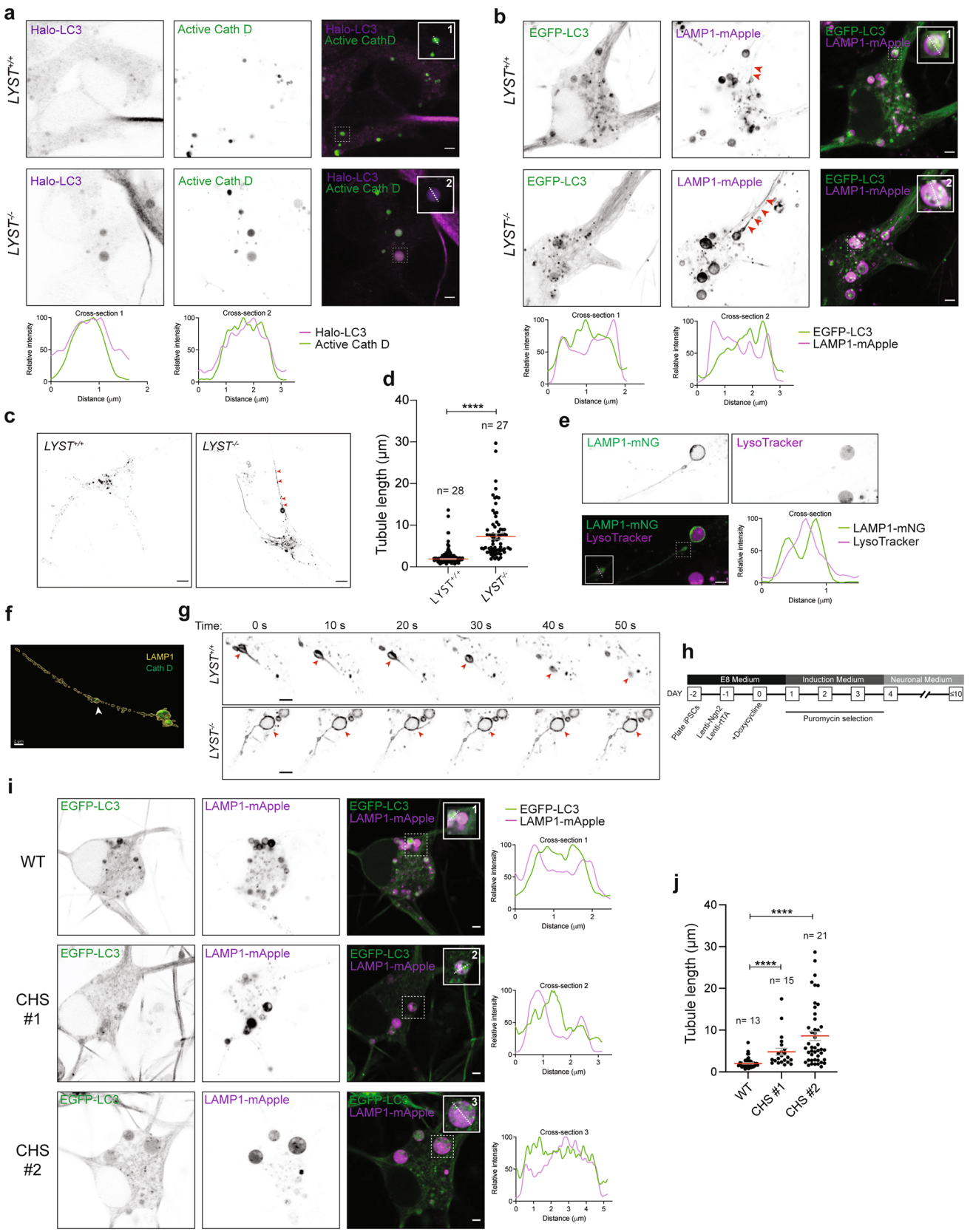
a
Halo-LC3
Active Cath D
Halo-LC3
Active CathD
LYST+/+
LYST-/-
Cross-section 1
Cross-section 2
Relative intensity
Distance (μm)
Halo-LC3
Active Cath D
b
EGFP-LC3
LAMP1-mApple
EGFP-LC3
LAMP1-mApple
c
LYST+/+
LYST-/-
d
Tubule length (μm)
****
n= 27
n= 28
e
LAMP1-mNG
LysoTracker
LAMP1-mNG
LysoTracker
Cross-section
f
LAMP1
Cath D
g
Time:
0 s
10 s
20 s
30 s
40 s
50 s
h
E8 Medium
Induction Medium
Neuronal Medium
DAY
Puromycin selection
Plate iPSCs
Lenti-Ngn2
Lenti-rtTA
+Doxycycline
i
WT
CHS #1
CHS #2
EGFP-LC3
LAMP1-mApple
Cross-section 1
Cross-section 2
Cross-section 3
j
Tubule length (μm)
****
****
n= 13
n= 15
n= 21
WT
CHS #1
CHS #2

◂**Fig. 2** LYST deficiency leads to abnormal autolysosome tabulation. **a** Upper panels show representative Airyscan images of *LYST*$^{+/+}$ and *LYST*$^{-/-}$ i^{3}Neurons expressing Halo-LC3 (purple). Cells were loaded with BODIPY-FL-pepstatin A (1 µM for 30 min) to label active forms of Cathepsin D (Cath D; green). Single-channel images are shown in inverted grayscale. Line-scan (in the lower panels) shows the related intensity profiles of Halo-LC3 (purple) and active Cath D (BODIPY-FL-pepstatin A; green) across the dotted line from the enlarged views. Scale bar 2 µm. **b** Upper panels show the representative Airyscan images of *LYST*$^{+/+}$ and *LYST*$^{-/-}$ i^{3}Neurons expressing EGFP-LC3 (green) and LAMP1-mApple (purple). Single-channel images are shown in inverted grayscale. Line-scan (in the lower panels) shows the related intensity profiles of EGFP-LC3 (green) and LAMP1-mApple (purple) across the dotted line from the enlarged views. Bafilomycin A1 (200 nM) was added to the media 3 h before data acquisition to avoid EGFP quenching in acidic pH. Red arrowheads in the LAMP1-mApple channel indicate the autolysosome tubules. Scale bar 2 µm. **c** Representative Airyscan images of *LYST*$^{+/+}$ and *LYST*$^{-/-}$ i^{3}Neurons expressing LAMP1-mNeonGreen. Images are shown in inverted grayscale. Red arrowheads show swollen structures in the middle of the autolysosome tubule. Scale bar 5 µm. See also Fig. S3a and Videos S1. **d** Quantitative analysis of autolysosome tubule lengths in *LYST*$^{+/+}$ and *LYST*$^{-/-}$ i^{3}Neurons presented as mean (in red) ± SEM with dots representing individual autolysosome tubule length contained in (*n*) number of analyzed cells from three independent experiments. ****$P < 0.0001$, unpaired two-tailed Mann–Whitney test. **e** Airyscan image showing autolysosome tubule in the *LYST*$^{-/-}$ i^{3}Neurons expressing LAMP1-mNeonGreen (mNG; green) and incubated with LysoTracker (purple). Lysotracker accumulated in the autolysosome lumen and in the bulge on the tubule (box region). This bulge is likely a nascent protolysosome that appears attached to the tubule and is acidic. Single-channel images are shown in inverted grayscale. Line-scan shows the related intensity profilers of LAMP1-mNG (green) and LysoTracker (purple) across the dotted line from the enlarged view. Scale bar 2 µm. See also Video S2. **f** Three-dimensional surface reconstruction from an Airyscan z-stack image of *LYST*$^{-/-}$ tubule extruding from an autolysosome immunostained with anti-LAMP1 antibody (yellow). The anti-Cath D (green) antibody immunostained the body of the autolysosome and the lumen of the putative protolysosome (white arrowhead). The fractional appearance of the autolysosome tubule is due to the paraformaldehyde fixation. Scale bar 2 µm. See also Fig. S3c. **g** Time-lapse images show how the autolysosome tubule modulates the movement of the autolysosome in *LYST*$^{+/+}$ and *LYST*$^{-/-}$ i^{3}Neurons expressing LAMP1-mNeonGreen. Images are shown in inverted grayscale. Red arrowheads point to the position of a specific autolysosome body at different time points. Scale bar 2 µm. See also Videos S1. **h** Scheme describing the iNeuron differentiation protocol used to differentiate iPSCs-derived from a healthy (wild type; WT) and two CHS patients. **i** Representative Airyscan images of iNeurons expressing EGFP-LC3 (green) and LAMP1-mApple (purple). iNeurons were differentiated from iPSCs-derived from a WT and two CHS patients. Single-channel images are shown in inverted grayscale. Line-scan shows the related intensity profiles of EGFP-LC3 (green) and LAMP1-mApple (purple) across the dotted line from the enlarged views. Scale bar 2 µm. **j** Quantitative analysis of autolysosome tubule length from a WT and two CHS patients' iNeurons, presented as mean (in red) ± SEM with dots representing individual autolysosome tubule lengths containing in (*n*) number of analyzed cells from three independent experiments. ****$P < 0.0001$, unpaired two-tailed Mann–Whitney test. See also Videos S3

using a micro-grooved Polydimethylsiloxane microdevice that provides a physical separation between the neuronal soma and their axons and allows parallel axonal extension suitable for imaging. The results revealed significantly less retrograde [*LYST*$^{+/+}$ (29.67 ± 1.94), *LYST*$^{-/-}$ (21.57 ± 1.28), $P < 0.01$] and anterograde [*LYST*$^{+/+}$ (51.43 ± 1.78), *LYST*$^{-/-}$ (46.64 ± 1.61), $P < 0.05$] along with more static events [*LYST*$^{+/+}$ (18.89 ± 1.29), *LYST*$^{-/-}$ (31.78 ± 1.71), $P < 0.0001$] in the *LYST*$^{-/-}$ i^{3}Neurons compared to the *LYST*$^{+/+}$ i^{3}Neurons (Fig. 1c, d). This finding suggests that LYST depletion diminishes lysosome transport in the neuronal axon but does not abolish their retrograde nor anterograde axonal transport. Our findings are in line with a previous report demonstrating that the interaction of lysosomes with a microtubule-dependent motor system is not altered by the absence of LYST [19].

LYST depletion alters the number of cathepsin D-positive organelles

The dysregulation of lysosomal degradation pathways is linked to various neurodegenerative disorders [20, 21]. The degradative lysosomes (autolysosomes or endolysosomes), which are mainly present in the neuronal soma, are characterized by the presence of lysosomal hydrolases, such as cathepsin D and B or ß-glucosidase in the lumen, surrounded by a membrane that contains LAMP1 [22, 23]. By indirect immunofluorescence using anti-LAMP1, anti-Cath D, and the neuronal marker anti-ß-tubulin III (TUBB3), we found a marked reduction [*LYST*$^{+/+}$ (21.72 ± 0.73), *LYST*$^{-/-}$ (6.72 ± 0.20), $P < 0.0001$] of Cath D-positive lysosomes (referring hereafter as lysosomes$_{CathD}$) in *LYST*$^{-/-}$ i^{3}Neurons, compared to the *LYST*$^{+/+}$ i^{3}Neurons (Fig. 1e, g). We verified that LAMP1 resides on the surface of the lysosomes$_{CathD}$, but not all the LAMP1-labeled organelles contain CathD (Fig. 1e, f). Therefore we used CathD immunostaining to differentiate the lysosomes$_{CathD}$ from the rest of LAMP1-positive organelles. When lysosomes$_{CathD}$ are analyzed by size (area) using a frequency distribution, *LYST*$^{-/-}$ i^{3}Neurons contained fewer small lysosomes$_{CathD}$ (< 0.4 µm) (Fig. 1h, histogram), and a higher number of very large lysosomes$_{CathD}$ (> 2 µm) (Fig. 1h, inset histogram) compared to the *LYST*$^{+/+}$ i^{3}Neurons. Comparable results were obtained in i^{3}Neurons derived from an independent *LYST*$^{-/-}$ iPSC-clone (Fig. S2a–c, clone #62B,) generated using a different combination of sgRNA. To further explore whether the loss of one allele of *LYST* produces a lysosome phenotype in neurons, we differentiated i^{3}Neurons from two heterozygous

($LYST^{+/-}$) iPSC clones (Fig. S2a–c, clone #7A and clone #63B); $LYST^{+/-}$ i^{3}Neurons did not have a significant reduction in the total number of lysosomes$_{CathD}$ (Fig. S2b) however, the analysis of their size (area) distribution showed a reduction in the number of small lysosomes$_{CathD}$ (< 0.4 µm) (Fig. S2c) and an increment in large lysosomes$_{CathD}$ with (> 2 µm) in $LYST^{+/-}$ i^{3}Neurons as compared to $LYST^{+/+}$ i^{3}Neurons (Fig. S2c, inset histogram). Taken together, our findings established that the lysosome phenotype in $LYST^{-/-}$ i^{3}Neurons is similar to the CHS cellular phenotype find in other cell types [10, 24–26], and provide the first evidence that loss of LYST function (total and partial) leads to a reduction of the number of the small lysosomes$_{CathD}$ and an increase in the number of large lysosomes$_{CathD}$ in neurons.

To further determine whether the reduction in the number of lysosomes$_{CathD}$ and their enlargement in size in $LYST^{-/-}$ i^{3}Neurons reflected changes in Cath D protein levels, we immunoblotted the total protein extracts using an anti-Cath D antibody that detects different forms of Cath D (Fig. S2d). Quantification of the ratio of proCath D to its mature two-chain enzyme form (Heavy chain/ProCath D) did not reveal any significant difference (Fig. S2e), suggesting that LYST deficiency does not alter the endolysosomal trafficking nor the maturation of lysosomal hydrolases, as reported previously [25].

The larger perinuclear lysosomes$_{Cath\ D}$ are autolysosomes

Autolysosomes are the sites where the degradation of intracellular cargo takes place following the fusion of autophagosomes with lysosomes during autophagy. Autolysosomes are characterized by the presence of the microtubule-associated protein light chain-3 (LC3), LAMP1, and Cath D. To determine whether enlarged Cath D positive compartments in the perinuclear region were autolysosomes, we transduced i^{3}Neurons with a lentivirus encoding the autophagic marker, LC3 fused to Halo-Tag (Halo-LC3) and loaded the cells with BODIPY-FL-pepstatin A, a fluorescent probe that binds specifically to active Cath D [27, 28] (Fig. 2a). The overlapping peaks between the intensity profiles of LC3 and active Cath D (BODIPY-FL-pepstatin A) confirmed their colocalization (Fig. 2a, lower panels: intensity profiles of Sect. 1 and 2). Next, we co-transduced the $LYST^{+/+}$ and $LYST^{-/-}$ i^{3}Neurons with EGFP-LC3 and LAMP1-mApple and we observed an enrichment of discrete EGFP-LC3-positive puncta that colocalized in the larger perinuclear LAMP1-mApple positive organelles (Fig. 2b, lower panels: intensity profiles of Sect. 1 and 2). Together, these results suggest that the large perinuclear Cath D positive organelles in both genotypes are autolysosomes.

LYST is necessary for the fission of protolysosomes from the autolysosome tubules

We observed the presence of tubular LAMP1-positive structures extruding from autolysosomes in both $LYST^{+/+}$ and $LYST^{-/-}$ i^{3}Neurons (Fig. 2b, red arrowheads in the LAMP1-mApple channel) which is indicative of the presence of ALR. To further evaluate the ALR in i^{3}Neurons, we transduced both $LYST^{+/+}$ and $LYST^{-/-}$ i^{3}Neurons with LAMP1-mNeonGreen and performed time-lapse live cell imaging. Of note, autolysosome tubules coming from $LYST^{-/-}$ i^{3}Neurons were remarkably longer compared to the $LYST^{+/+}$ i^{3}Neurons [$LYST^{+/+}$ (2.31 ± 0.15), $LYST^{-/-}$ (7.76 ± 0.68), $P < 0.0001$] (Figs. 2c, d, S3a and Videos S1). However, the percentage of LAMP1-positive tubules was not significantly different between both genotypes, which indicates that the initiation of the autolysosome tubules was not affected by LYST depletion (Fig. S3b). Additionally, we noticed frequently swollen structures in the middle of the autolysosome tubule in the $LYST^{-/-}$ i^{3}Neurons (Fig. 2c, red arrowheads). These swollen structures are acidic (Fig. 2e and Video S2) and proteolytically active (Figs. 2f, white arrowhead and S3c) and may represent nascent protolysosomes that were not released from the autolysosome tubule during ALR. Moreover, it appeared that the autolysosome tubule in $LYST^{+/+}$ i^{3}Neurons helped in pulling autolysosomes through the cellular soma. However, in $LYST^{-/-}$ i^{3}Neurons, the autolysosome tubules were more static and did not appear to promote autolysosome mobility (Fig. 2g and Video S1). Despite the longer tubules extruding from the autolysosomes in $LYST^{-/-}$ i^{3}Neurons, these autolysosomes maintained their degradative capacity as gauged by DQ-BSA (Fig. S4a), and acidic pH confirmed by the LysoTracker staining of the LAMP1-positive structures in both genotypes (Fig. S4b). Their acidification was also reported by the presence of active proteases: Cath B (Magic Red-Cath B; Fig. S4c) and, as mentioned previously, Cath D (Fig. 2a, active Cath D).

To determine if LYST plays a role in autophagy, we evaluated the levels of cytosolic LC3-I and its lipidated form LC3-II, which is recruited to the autophagosome membranes where it is eventually internalized upon autolysosome formation to be degraded by lysosomal hydrolases. The levels of LC3 in i^{3}Neurons were evaluated with and without Bafilomycin A1 (Baf A1; 200 nM for 3 h), a reversible inhibitor of lysosome H^+-ATPase that inhibits acidification, and therefore protein cargo degradation during autophagy. We found that the levels of LC3-I and II were similar in both genotypes (Fig. S4d–g), which indicates that LYST depletion does not increase autophagosome formation nor reduce autolysosome clearance. Similarly, we did not find any significant difference between genotypes in the protein levels of SQSTM1/p62 (Figs. S4d and S4h), an adaptor that links

ubiquitinated cargo to the LC3 machinery during engulfment. Taken together, these results indicate that the absence of LYST does not affect autophagy.

CHS iPSCs-derived iNeurons phenocopy LYST$^{-/-}$ i^{3}Neurons

We differentiated two of our previously characterized CHS iPSC lines [29] together with an unrelated healthy iPSCs (wild-type; WT), into glutamatergic neurons using lenti-*Ngn2* (neurogenin-2) and lenti-rtTA (reverse tetracycline-controlled trans-activator) [30]. These neurons are subsequently referred to as iNeurons (protocol scheme Fig. 2h). Using lentivirus encoding EGFP-LC3 and LAMP1-mApple, we confirmed that the larger perinuclear LAMP1-mApple positive organelles are indeed autolysosomes (Fig. 2i). By monitoring autolysosome tubulation using LAMP1-mNeonGreen, we also showed that CHS iNeurons exhibited longer tubules compared to WT iNeurons (Fig. 2j and Videos S3), however the percentage of LAMP1-positive tubules in iNeurons was not significantly different between genotypes (Fig. S4i). These results demonstrate that the lysosomal phenotype in *LYST*$^{-/-}$ i^{3}Neurons is reminiscent of the lysosomal phenotype in the CHS patient-derived iNeurons.

Exogenous LYST expression increases the number of small lysosomes$_{CathD}$ and reduces the number of large lysosomes$_{CathD}$ in *LYST*$^{-/-}$ i^{3}Neurons

To further underscore the role of LYST, we aimed to overexpress the exogenous *LYST* in both *LYST*$^{-/-}$ and *LYST*$^{+/+}$ i^{3}Neurons. However, the enormous size of *LYST* cDNA (11.4 kb) posed difficulty for its delivery into cells and its exogenous expression. Therefore, we utilized the piggyBac transposon system (Fig. 3a), a non-viral genetic engineering system that allows the introduction of the large open reading frame into the genome [31–33]. Using this system, we were able to introduce the piggyBac cargo, composed of LYST tagged with ALFA-tag (LYST-ALFA) and a selection cassette that conferred resistance to hygromycin and mNeonGreen fused to a Nuclear Localization Signal (NLS) in the genome of *LYST*$^{+/+}$ and *LYST*$^{-/-}$ iPSCs (Fig. 3b, c). Following the differentiation of iPSCs to i^{3}Neurons, the total level of *LYST* mRNA was two-fold higher in *LYST*$^{+/+}$ i^{3}Neurons overexpressing LYST-ALFA compared to *LYST*$^{+/+}$ i^{3}Neurons. The level of exogenous *LYST* mRNA in *LYST*$^{-/-}$ i^{3}Neurons overexpressing LYST-ALFA was comparable to the level in *LYST*$^{+/+}$ i^{3}Neurons (Fig. 3d). Using an anti-ALFA nanobody we were able to detect the LYST-ALFA construct by the western blotting (Fig. 3e). Through indirect immunofluorescence of Cath D, we demonstrated that the increased expression of LYST led to a significant increase in the number of lysosomes$_{CathD}$ in *LYST*$^{-/-}$ i^{3}Neurons and a modest increment in *LYST*$^{+/+}$ i^{3}Neurons (Fig. 3f, g). The increased number of lysosomes$_{CathD}$ in *LYST*$^{-/-}$ i^{3}Neurons overexpressing LYST-ALFA was noticeable in the small lysosomes$_{CathD}$ (< 0.4 µm) fraction, where we observed a three-fold higher number of small lysosomes$_{CathD}$ (423 in *LYST*$^{-/-}$ vs 1321 in *LYST*$^{-/-}$ overexpressing LYST-ALFA; Fig. 3h, # in the histogram). Interestingly, the increased LYST expression also reduced the number of the larger lysosomes$_{CathD}$ (> 2 µm) in the *LYST*$^{-/-}$ i^{3}Neurons background (Fig. 3h, inset histogram). These results suggest that LYST plays an important role in maintaining lysosomal homeostasis, likely by promoting the protolysosome generation from the fission of autolysosome tubules during ALR. Unfortunately, our attempts to determine if LYST is localized to lysosomal domains to mediate the fission failed, likely because the levels of the exogenous *LYST* in i^{3}Neurons are not enough to be detectable by immunofluorescence (IF).

Exogenous *LYST* expression restores the lysosomes$_{CathD}$ pool during autophagy

We next investigated whether the expression of LYST-ALFA can be increased using other cells, such as the osteosarcoma cell line (U2OS), which offers efficient transfection and flattened cell morphology for IF analysis. *LYST* is endogenously expressed at lower levels in U2OS cells (www.proteinatlas.org), however stable transfection of LYST-ALFA in U2OS (Fig. 4a) led to a robust increase of *LYST* mRNA (Fig. 4b) that was markedly higher than in LYST-overexpressed i^{3}Neurons (Fig. 4c). In agreement with increased mRNA expression, we also found noticeably higher exogenous LYST-ALFA protein levels in U2OS as compared to both iPSC and i^{3}Neurons (Fig. 4d). Consistent with our findings in i^{3}Neurons, we observed a significantly increased number of small lysosomes$_{CathD}$, possibly protolysosomes, in U2OS overexpressing LYST-ALFA compared to mock-transfected cells (ALFA) under basal (growth media; GM) conditions (Fig. 4e, f, GM panels). Next, we evaluated the effect of LYST overexpression in U2OS cultured for 24 h in Earle's balanced salt solution (EBSS), which is known to induce autophagy [34, 35]. During autophagy, peripheral lysosomes are redistributed toward the perinuclear region of the cell to promote membrane fusion between lysosomes and autophagosomes. Consistent with this, ALFA U2OS cells growing in EBSS exhibited noticeably larger and perinuclearly clustered lysosomes$_{CathD}$ compared to the cells growing in GM, which led to a reduction in the lysosomes$_{CathD}$ puncta per cell (Fig. 4e, f, ALFA cells panels). Conversely, in U2OS cells overexpressing LYST-ALFA, there were noticeably smaller and more abundant lysosomes$_{CathD}$ scattered in the cell periphery (in both GM and EBSS) compared to ALFA cells (Fig. 4e, f). These results show that exogenous LYST

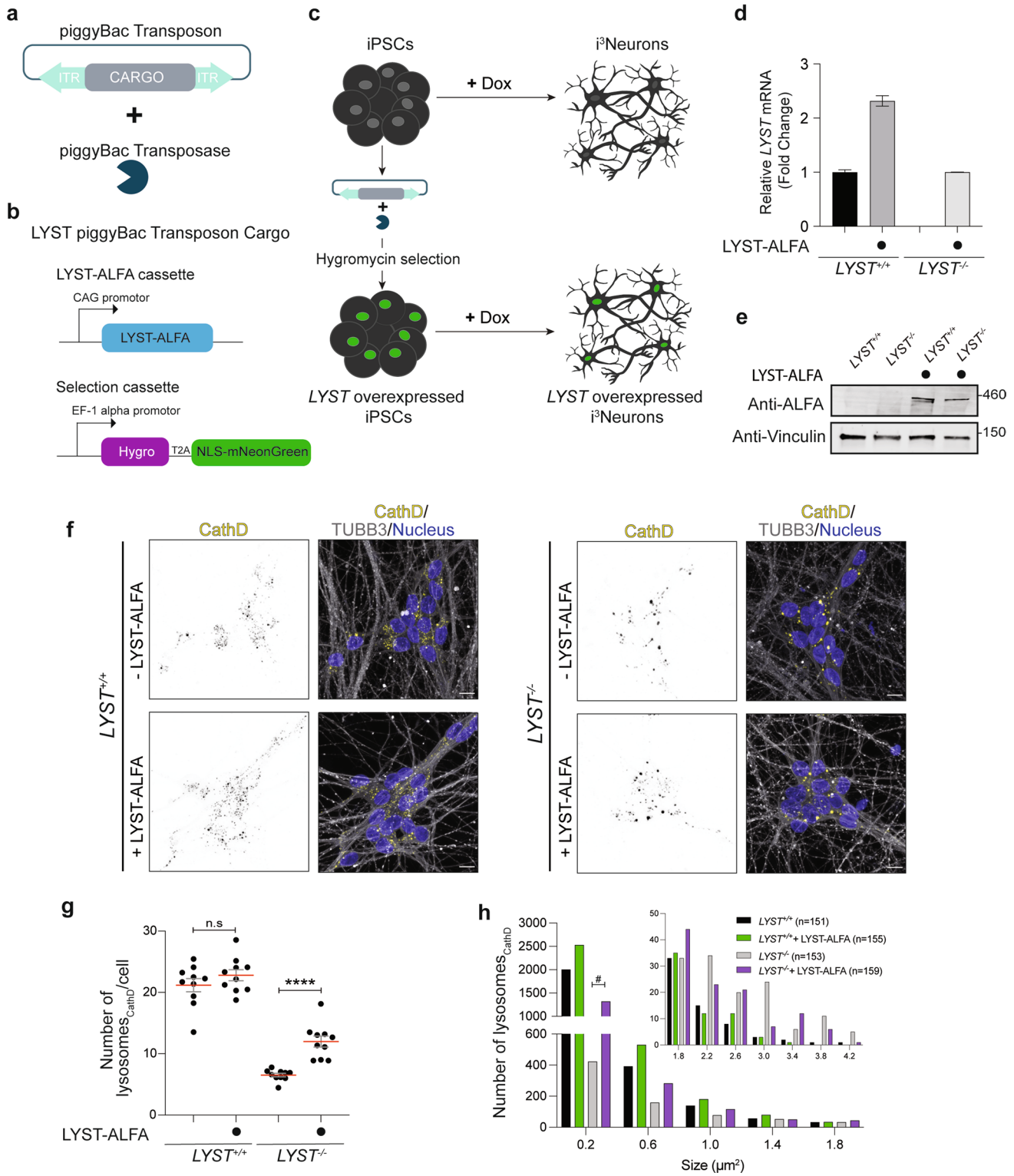

increases the formation of small lysosomes$_{CathD}$ in both GM and EBSS media and supports the probable role of LYST in maintaining the lysosome pool (lysosomal homeostasis) even in autophagy conditions, where there is a reduction of the number of free lysosomes. As expected, LC3-II levels were increased in cells growing in EBSS compared to GM (Fig. 4g, h), confirming successful starvation-induced autophagy in cells expressing both ALFA and LYST-ALFA. After the treatment of cells with Baf A1, which blocks the degradation of the autolysosome contents by the lysosomal hydrolases'

◂**Fig. 3** LYST overexpression increases the number of lysosomes$_{CathD}$. **a** Scheme of the piggyBac system that consists of piggyBac transposon and transposase vector, which transiently expresses the transposase enzyme that integrates the transposon cargo into the genome. The transposase allows the integration of the transposon cargo into random TTAA genomic DNA location by the recognition of the transposon-specific inverted terminal repeat sequences (ITRs) flanking the transposon cargo. **b** Transposon cargo is composed of two separate cassettes, each consisting of different promotors. Top: The CAG promoter drives the expression of LYST cDNA fused with ALFA-tag (LYST-ALFA). Bottom: The EF-1 alpha promoter controls the selection cassette that confirms resistance to hygromycin and mNeonGreen fussed to a Nuclear Localization Signal (NLS). **c** Strategy for the generation of stable *LYST* overexpressed i^{3}Neurons. The LYST-ALFA transposon was co-transfected with the transposase in *LYST*$^{+/+}$ and *LYST*$^{-/-}$ iPSCs. After 72 h, cells were selected with hygromycin to generate iPSCs that stably express LYST-ALFA. *LYST*$^{+/+}$ and *LYST*$^{-/-}$ iPSCs were differentiated into i^{3}Neurons by the addition of doxycycline in the media. **d** A representative qPCR experiment and quantification of the relative fold change of *LYST* mRNA levels in *LYST*$^{+/+}$ and *LYST*$^{-/-}$ i^{3}Neurons expressing LYST-ALFA as compared to a *LYST*$^{+/+}$ and *LYST*$^{-/-}$ i^{3}Neurons. Values are the mean ± SEM. Each sample was run in triplicates. **e** Total protein extracts of *LYST*$^{+/+}$ and *LYST*$^{-/-}$ i^{3}Neurons were analyzed by western blotting using anti-ALFA nanobody. Vinculin was used as a loading control. The positions of molecular mass markers (in kDa) are indicated on the right side. **f** Representative images of *LYST*$^{+/+}$ and *LYST*$^{-/-}$ i^{3}Neurons without and with the expression of LYST-ALFA showing the indirect immunofluorescence of cathepsin D (Cath D; yellow). The grey color represents ß-tubulin III (TUBB3). Cell nuclei were visualized using Hoechst 33342 (in blue) because after fixation NLS-mNeonGreen was not visible. Single-Cath D channel images are shown in inverted grayscale. Scale bar 10 µm. **g** Quantification of lysosome$_{CathD}$ per cell presented as mean (in red) ± SEM with dots representing the average of lysosome$_{CathD}$/cell per image analyzed. Two independent differentiation experiments were performed and 10 images per genotype were analyzed, representing a total of > 150 cells per genotype. ****$P < 0.0001$; *ns* nonsignificant, unpaired two-tailed Mann–Whitney test. **h** Histograms showing lysosomes$_{CathD}$ size (area) distribution. Data were pooled from a similar number (*n*) of cells from each i^{3}Neurons genotype as shown. The bin width is 0.4 µm^2. The distribution of sizes is presented in two separate histograms; the histogram shows the number of lysosomes$_{CathD}$ up to 2.0 µm^2 area, and the histogram in the inset shows the distribution of lysosomes$_{CathD}$ with the larger area, ranging between 1.6 to 4.4 µm^2. The symbol # indicates a three-fold increase in lysosomes$_{CathD}$ number (< 0.4 µm) in *LYST*$^{-/-}$ i^{3}Neurons expressing LYST-ALFA compared to *LYST*$^{-/-}$ i^{3}Neurons

inactivation, there is a significant increase of the LC3-II levels in all the conditions (lanes 5–8), which reflects a reduction of autolysosome clearance due to the lysosome de-acidification. Our results suggest that the LYST-ALFA exogenous expression does not affect autolysosome clearance. Additionally, using the anti-ALFA nanobody, we detected an increment of LYST expression when LYST-ALFA cells were grown in EBSS for 24 h (Fig. 4g, i, compare lanes 3 and 4). This is likely an effect of nutrient deprivation on the CAG promoter activity [36], causing an increase in LYST-ALFA mRNA levels (Fig. 4j). LYST-ALFA is slightly increased in the Baf A1 treatment (Fig. 4g, i), which suggests that its degradation is also reduced due to lysosomal de-acidification.

To explore if ALR defects in LYST-depleted i^{3}Neurons affect their viability after long-term starvation [37], we cultured *LYST*$^{+/+}$ and *LYST*$^{-/-}$ i^{3}Neurons in EBSS for 24 h. We noticed a slight reduction of lysosomes$_{CathD}$ number (Figs. S5a and S5b). The distribution of the lysosomes$_{CathD}$ by their size (area) revealed a reduction of 18% and 36% in the number of small lysosomes$_{CathD}$ (< 0.4 µm) in *LYST*$^{+/+}$ and *LYST*$^{-/-}$ i^{3}Neurons, respectively (Fig. S5c), suggesting that LYST is important for the repopulation of these small lysosomes$_{CathD}$, possibly corresponding to protolysosome fraction, in autophagy conditions (EBSS). Moreover, the viability of the *LYST*$^{-/-}$ i^{3}Neurons was comparable to *LYST*$^{+/+}$ i^{3}Neurons under prolonged nutrient deprivation (Fig. S5d), suggesting that LYST depletion does not affect the survival of i^{3}Neurons in prolonged starvation.

LYST is recruited to LAMP1-positive structures to maintain lysosomal homeostasis

Using ALFA nanobody, we detected diffuse staining in the cytoplasm of U2OS cells expressing LYST-ALFA (Fig. 5a). This finding is consistent with a previous report [11] and suggests that LYST may be localized in the cytoplasm. Additionally, LYST-ALFA was also recruited to specific donut shaped-structures (Fig. 5a, red arrowhead). Localization of LYST to similar structures has been described in other non-mammalian *LYST* orthologs, including *Dictyostelium lvsB* [10] and the *Drosophila* Mauve [38]. Moreover, compared to cells in GM, these structures increased in size after growing cells in EBSS media for 24 h with distinctly higher fluorescence intensity compared to cells growing in GM (Fig. 5a, right-intensity panel), possibly due to the higher LYST-ALFA levels in EBSS. Interestingly even with the differences in the LYST-ALFA levels between GM and EBSS, LYST-ALFA followed the same structural recruitment pattern suggesting a very specific LYST localization. This is further supported by our observation that donut-shaped structures were not detected in mock cells (Fig. S6a).

Co-staining the cells with anti-ALFA nanobody and anti-LAMP1 antibody revealed a high degree of colocalization in big and perinuclear LAMP1-positive lysosomes that are aggregated (Fig. 5b, top panel) or make tubulation events (Fig. 5b, bottom panel). To provide additional evidence that LYST is localized in the direct vicinity of the LAMP1-positive structures to mediate their fission, we performed a proximity labeling assay. We generated a lentiviral construct in which LAMP1-3xFLAG was fused to engineered ascorbate peroxidase 2 (APEX2) [39]. We transduced U2OS cells expressing LYST-ALFA with the lenti-LAMP1-3xFLAG-APEX2 to generate a stable cell line that expresses both LYST-ALFA and LAMP1-3xFLAG-APEX2. First, we assessed APEX2 functionality (Fig. S6b) and we also confirmed

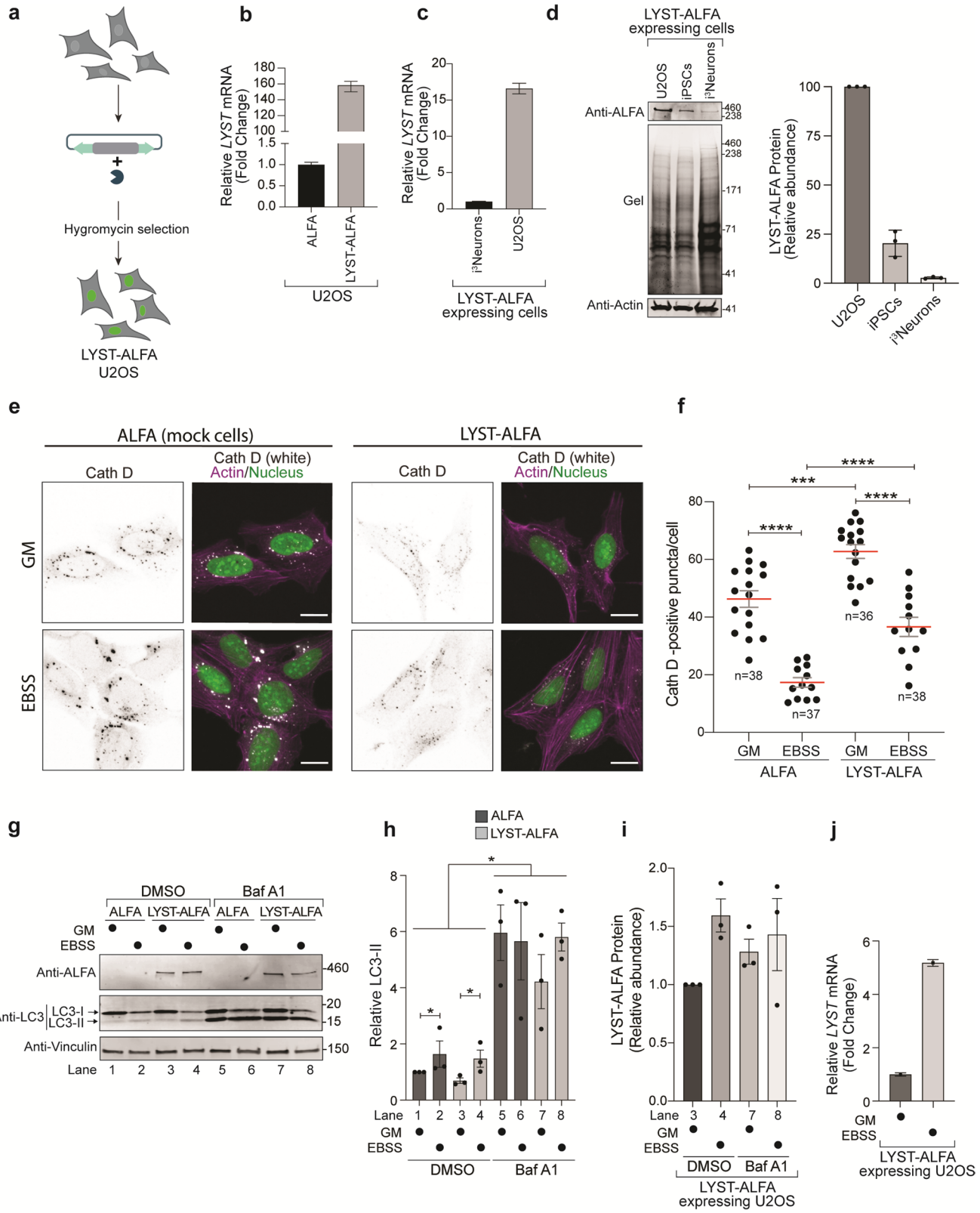

that LAMP1-3xFLAG-APEX2 colocalized with the endogenous LAMP1 (Fig. S6c). Next, we cultured cells in either GM or EBSS for 24 h, and we started the APEX2 reaction by incubating cells with biotin-phenol. Following the addition of hydrogen peroxide (H_2O_2) for 1 min, APEX2 catalyzed the oxidation of biotin-phenol to a highly reactive

◂**Fig. 4** LYST overexpression restores the number of lysosomes$_{CathD}$ during autophagy. **a** Strategy for generating a stable LYST overexpressed U2OS line. The LYST-ALFA transposon was co-transfected with the transposase in U2OS cells. After 72 h, cells were selected with hygromycin to generate a stable LYST-ALFA overexpressed U2OS line. **b** A representative qPCR experiment and quantification of the relative fold change of *LYST* mRNA levels in U2OS expressing LYST-ALFA as compared to U2OS expressing the piggyBac with only ALFA-tag (ALFA, mock cells). Values are the mean ± SEM. Each sample was run in triplicate. **c** A representative qPCR experiment and quantification of the relative fold change of *LYST* mRNA levels in i^{3}Neurons and U2OS, both expressing LYST-ALFA. Values are the mean ± SEM. Each sample was run in triplicates. **d** Total protein extracts of U2OS, iPSC, and i^{3}Neurons expressing LYST-ALFA were analyzed by western blotting using anti-ALFA nanobody. Actin was used as a loading control. Positions of molecular mass markers (in kDa) are indicated on the right side. The image of the stain-free gel before protein transfer shows that a similar amount of protein lysates was loaded. On the right, the quantitative analysis of the total LYST-ALFA levels is shown. Each band intensity was normalized to the actin band intensity of the same sample. Values are represented as mean ± SEM from three independent experiments. Representative images of ALFA U2OS (mock cells) and LYST-ALFA U2OS showing the indirect immunofluorescence of the cathepsin D (Cath D; white) and the ß-tubulin III (TUBB3; purple). Single-Cath D channel images are shown in inverted grayscale. The cell nuclei were visualized by the expression of mNeonGreen from the piggyBac transposon selection cassette, indicating stable expression after fixation. Cells were cultured in growth media (GM, upper panels) or in EBSS for 24 h (lower panels). Scale bar 20 µm. **f** Quantification of Cath D-positive puncta per cell presented as mean (in red) ± SEM with dots representing the average Cath D-positive puncta per image analyzed. A total of 12–16 images per genotype and condition (GM or EBSS) were analyzed representing a total of (n) number of cells. ***$P < 0.001$; ****$P < 0.0001$, unpaired two-tailed Mann–Whitney test. **g** Total protein extracts of U2OS expressing ALFA (mock cells) and LYST-ALFA cultured in GM or EBSS for 24 h were analyzed by western blotting using anti-LC3 antibody and anti-ALFA nanobody. Bafilomycin A1 (Baf A1) treatment was carried out for 3 h at 200 nM. Vinculin was used as a loading control. Anti-LC3 antibody revealed two bands; the upper band is LC3-I, and the lower band is LC3-II (lipidated LC3). The positions of molecular mass markers (in kDa) are indicated on the right side. **h**, **i** Quantitative analysis of total LC3-II relative to the total LC3-II levels in ALFA U2OS in GM treated with DMSO (**h**) and total LYST-ALFA protein levels relative to the total LYST-ALFA levels in LYST-ALFA U2OS in GM treated with DMSO (**i**). Each band intensity was normalized to the vinculin band intensity of the same sample. Values are represented as mean ± SEM ($n = 3$). *$P < 0.05$, unpaired Mann–Whitney test. **j** A representative qPCR experiment and quantification of the relative fold change of *LYST* mRNA levels in U2OS expressing LYST-ALFA in GM or EBSS media. Values are the mean ± SEM. Each sample was run in triplicates

biotin-phenoxyl radical, which conjugated to proteins that are proximal to the LAMP1-3xFLAG-APEX2. We then used streptavidin beads to pull down biotinylated proteins and analyzed them by western blotting using anti-ALFA nanobody (Fig. 5c). We detected LYST-ALFA as a protein near LAMP1-3xFLAG-APEX2. Next, we calculated band intensities of biotinylated LYST-ALFA and LAMP1-3xFLAG-APEX2 in streptavidin pull down. We found a higher LYST-ALFA/LAMP1-3xFLAG-APEX2 ratio in EBSS compared to GM (Fig. 5d, e), suggesting more recruitment of LYST-ALFA in LAMP1-positive structures during autophagy. These results support the assumption that LYST is associated with or nearby the lysosome membrane (LAMP1-positive structures) in both basal (GM) and during autophagy conditions (EBSS). Overall, these results suggest that LYST is preferentially recruited to LAMP1-positive structures to mediate lysosome-associated membrane events such as ALR.

Discussion

During autophagy, there is a rapid decline in the number of lysosomes owing to their fusion with autophagosomes to form autolysosomes in the perinuclear region of the cells. ALR commences at the termination of autophagy to restore the pool of functional lysosomes [1]. The ALR process can be divided into four steps: (1) initiation of the tubular structures from autolysosomes; (2) tubule elongation by the coordination of actin polymerization and the kinesin 5B [40] that mediates the tubule extension along microtubules; (3) scission of protolysosomes, and; (4) the protolysosome maturation. The impairment in ALR due to a defect in initiation results in enlarged autolysosomes accompanied by a lysosome depletion [41–44]**.** In addition to the enlarged autolysosomes and the lysosome depletion, the autolysosome tubules became hyperelongated when the impairment is due to disruption of the autolysosome tubule scission [37, 45, 46]**.** In *LYST*$^{-/-}$ i^{3}Neurons, we observed a remarkable reduction in the number and increment in the size of lysosomes$_{CathD}$ accompanied by hyperelongated autolysosome tubules. The elongated tubules feature a 'beads on necklace' appearance in which beads may represent newly immerging protolysosomes that remained attached to the LAMP1-positive tubule. We hypothesized that LYST is required for mediating the scission/fission of protolysosomes to bud off from the autolysosome tubule and ultimately restore the lysosome pool after autophagy (Fig. 6). In support of this notion, we observed (i) an increment in the number of the small lysosomes$_{CathD}$ fraction, probably protolysosomes, when *LYST* was exogenously expressed in the *LYST*$^{-/-}$ i^{3}Neurons and in U2OS cells; (ii) in autophagy-induction media (EBSS) when there is a rapid decline in lysosomes$_{CathD}$, the overexpression of LYST-ALFA was able to reverse the lysosomes$_{CathD}$ pool depletion; and (iii) an increased localization of LYST in a proximal region of LAMP1-positive structures/lysosomes in basal and autophagy conditions (Fig. 6, II+, LYST in red spheres). While our results support LYST as a positive regulator of lysosome fission or more precisely a positive regulator of the fission of autolysosome tubules, we cannot formally rule out the possibility that LYST may also

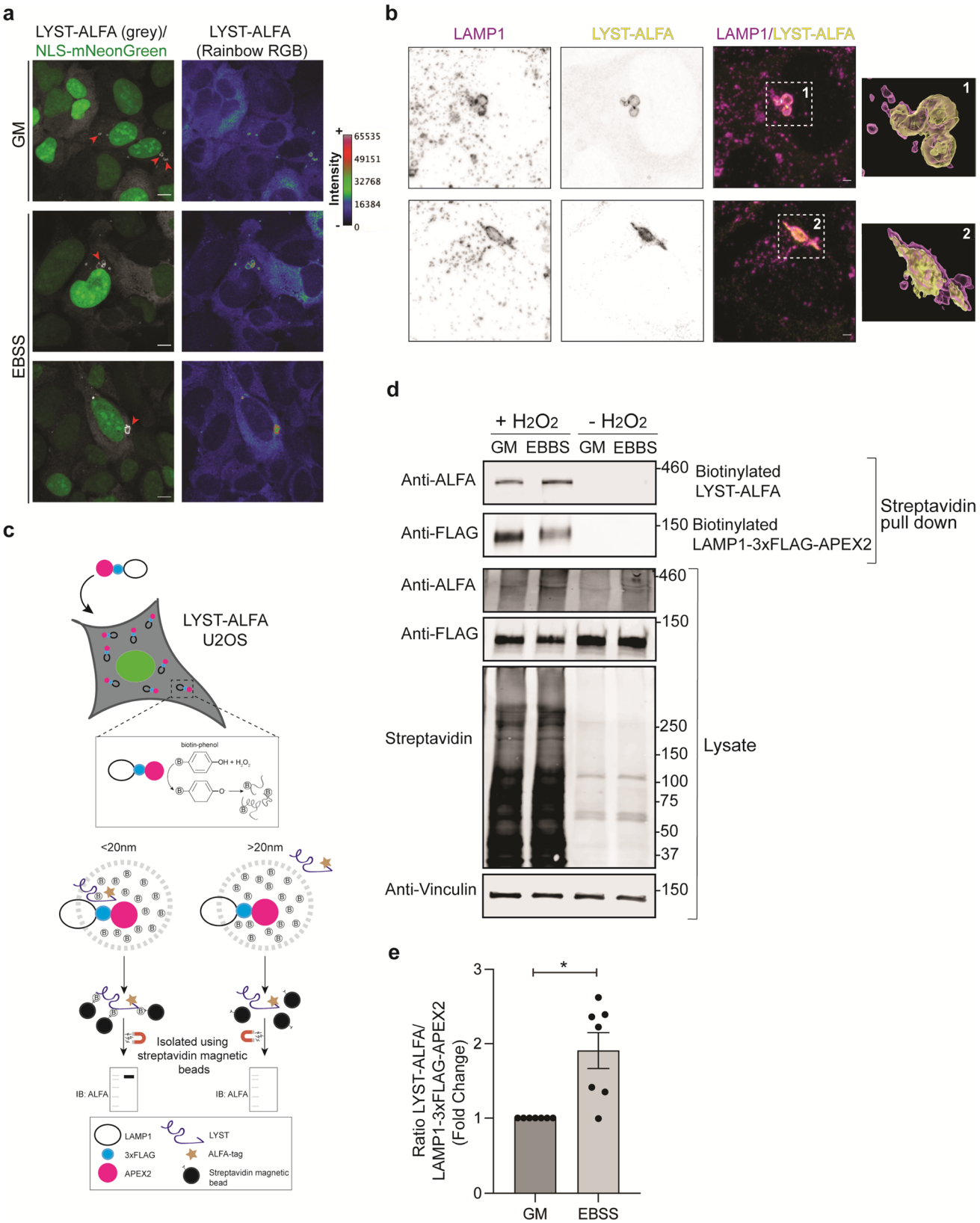
a
LYST-ALFA (grey)/
NLS-mNeonGreen
LYST-ALFA
(Rainbow RGB)
GM
EBSS
Intensity
65535
49151
32768
16384
0
b
LAMP1
LYST-ALFA
LAMP1/LYST-ALFA
1
2
c
LYST-ALFA
U2OS
biotin-phenol
<20nm
>20nm
Isolated using
streptavidin magnetic
beads
IB: ALFA
IB: ALFA
LAMP1
3xFLAG
APEX2
LYST
ALFA-tag
Streptavidin magnetic
bead
d
+ H2O2
- H2O2
GM EBSS GM EBSS
Anti-ALFA
Anti-FLAG
Biotinylated
LYST-ALFA
Biotinylated
LAMP1-3xFLAG-APEX2
Streptavidin
pull down
Anti-ALFA
Anti-FLAG
Streptavidin
Anti-Vinculin
Lysate
460
150
250
150
100
75
50
37
e
Ratio LYST-ALFA/
LAMP1-3xFLAG-APEX2
(Fold Change)
*
GM
EBSS

◂**Fig. 5** LYST is localized to LAMP1-positive structures. **a** U2OS expressing LYST-ALFA were cultured either in growth media (GM) or in EBSS for 24 h. Indirect immunofluorescence using anti-ALFA shows donut-shaped structures (red arrowheads). LYST-ALFA is grey on the left panel and with Rainbow RGB LUT to visualize the fluorescence intensity on the right panel. The cell nuclei were visualized by the expression of mNeonGreen from the piggyBac transposon selection cassette, indicating stable expression after fixation. Scale bar 10 µm. The calibration bar on the right of the figure shows the fluorescence intensity. See also Fig. S6a. **b** Two representative Airyscan images of U2OS expressing LYST-ALFA. The left panels show the immunostaining using an anti-LAMP1 antibody (purple) and anti-ALFA nanobody (yellow). Single-channel images are shown in inverted grayscale. The right panels show the three-dimensional surface reconstruction from an Airyscan z-stack image of the indirect immunofluorescence of LAMP1 (purple) and ALFA (yellow) from regions 1 and 2. Scale bar 2 µm. **c** Schematic of APEX2 proximity labeling assay. U2OS expressing LYST-ALFA were transduced with lenti-LAMP1-3xFLAG-APEX2. APEX2 is an engineered peroxidase that uses biotin-phenol and hydrogen peroxide (H_2O_2) to produce highly reactive biotin-phenol radicals that covalently biotinylated proteins that are up to 20 nm in distance. Biotinylated proteins can be enriched from lysates using streptavidin beads and only if LYST-ALFA is nearby 20 nm of distance to LAMP1-3xFLAG-APEX2, it will be detectable using anti-ALFA nanobody. **d** Cells were cultured either in growth media (GM) or in EBSS for 24 h and induced with H_2O_2 for 1 min before lysis. Biotinylated proteins were enriched from lysates using streptavidin beads and immunoblotted using anti-ALFA nanobody and anti-FLAG antibody (to detect LAMP1-3xFLAG-APEX2). Detection of LYST-ALFA band (below 460 kDa molecular weight marker) suggests that LYST is present within 20 nm of LAMP1 positive structures (top panels). Uninduced cells (without the addition of H_2O_2) were used as a negative control. Lysates show the expression of LYST-ALFA and LAMP1-3xFLAG-APEX2 proteins (bottom panels). Streptavidin conjugated to infrared dye 680 was used for detecting biotinylated proteins. Vinculin was used as a loading control. See also Figs. S6b and S6c. **e** Quantitative analysis of LYST-ALFA recruitment or proximal to the LAMP1-3xFLAG-APEX2 after streptavidin pull down and immunoblotting with anti-ALFA nanobody and anti-FLAG antibody. Ratio of LYST-ALFA/LAMP1-3xFLAG-APEX2 was calculated from each pull down. Values are presented as mean ± SEM from 7 independent experiments. $^*P < 0.05$, unpaired two-tailed Mann–Whitney test

regulate lysosome fusion events. In addition to deficient ALR, the enlarged autolysosomes in *LYST*$^{-/-}$ i^{3}Neurons could be an additional consequence of the fusion of the remaining free functional lysosomes to maintain autolysosome degradative capability (Fig. 6, V). This scenario could explain why the *LYST*$^{-/-}$ autolysosomes maintain their degradative function as well as their acidic pH.

Our observation regarding the loss of one *LYST* allele (*LYST*$^{+/-}$) also led to an effect on lysosome size and number further underscoring that LYST regulates the lysosomes$_{CathD}$ size and number in a dose-dependent manner. However, because the CHS symptomatology is not reported in *LYST* heterozygotes, we assume that even if we were able to detect a cellular effect upon partial loss of LYST function, this effect is not clinically pathogenic.

In this study, we have not been focused on the possible mechanisms that could help us to underscore the neurological phenotype seen in CHS patients. However, efficient and constitutive autophagy is particularly important in neurons [47, 48] to preserve their homeostasis. Autophagy dysfunction has been extensively linked to neurodegeneration and impaired neurological function [49]. Furthermore, several studies linked ALR dysfunction with neurodegenerative diseases, such as hereditary spastic paraplegia [42, 50–52] and Parkinson's disease [53, 54]. In *LYST*$^{-/-}$ i^{3}Neurons, we did not find evidence for autophagy-induced cell death, possibly because autophagy is highly a cell/tissue-dependent process [48, 49] and cortical glutamatergic neurons, such as the i^{3}Neurons, may be more resistant in displaying the pathological consequences compared to other brain cells. The loss of cerebellar Purkinje cells has been documented in *Lyst*-mutant mice [14–16]. Purkinje cells are very susceptible to the consequences of compromised autophagy [55]. Therefore, the loss of Purkinje cells may be a consequence of primary defects in ALR and the cell's ability to withstand them.

Our results also suggest that autolysosome tubules may help in the mobility of autolysosomes through the soma; the hyperelongated autolysosome tubules in *LYST*$^{-/-}$ i^{3}Neurons are likely hindering this movement. However, we don't know the biological consequences of this phenomenon or if this can also explain the presence of more static lysosomes in the neuronal axons.

The main hallmark of CHS is immunological dysfunction, therefore, it could be attractive to investigate how LYST operates in the lysosomal tubulation observed during the activation of immune cells. Interestingly, lysosomes in bone marrow-derived macrophages from *beige* mice showed abnormal tubular morphology [12] resembling the autolysosome tubules seen in *LYST*$^{-/-}$ neurons. These observations indicate that LYST and its possible partners could operate similarly to regulate ALR in different cell types. Additionally, LROs share features with the endolysosome system, and their function is cell-type-specific [56]. Melanosomes (LROs of skin epidermal melanocytes and eye-pigmented cells) reshape their membrane to form melanosome-recycling tubules that ultimately undergo fission. Defects in the fission of these tubules may result in the loss of organelle homeostasis and increased organelle size [57]. The architectural similarity between the melanosome recycling tubules and ALR, as well as the large melanosomes seen in CHS melanocytes, maybe a consequence of the loss of LYST function in coordinating the melanosome recycling by tubules pinch-off. Therefore, future studies should focus on the LYST-mediated mechanism that regulated the scission of protolysosomes from the autolysosome tubules during ALR to further understand the CHS symptomatology and the role of LYST in LRO biology. However, the enormous size of LYST continues to pose a technical challenge to precisely dissecting its role. Our LYST-deficient human neuronal cell model and the piggyBac transposon system to express *LYST* in different

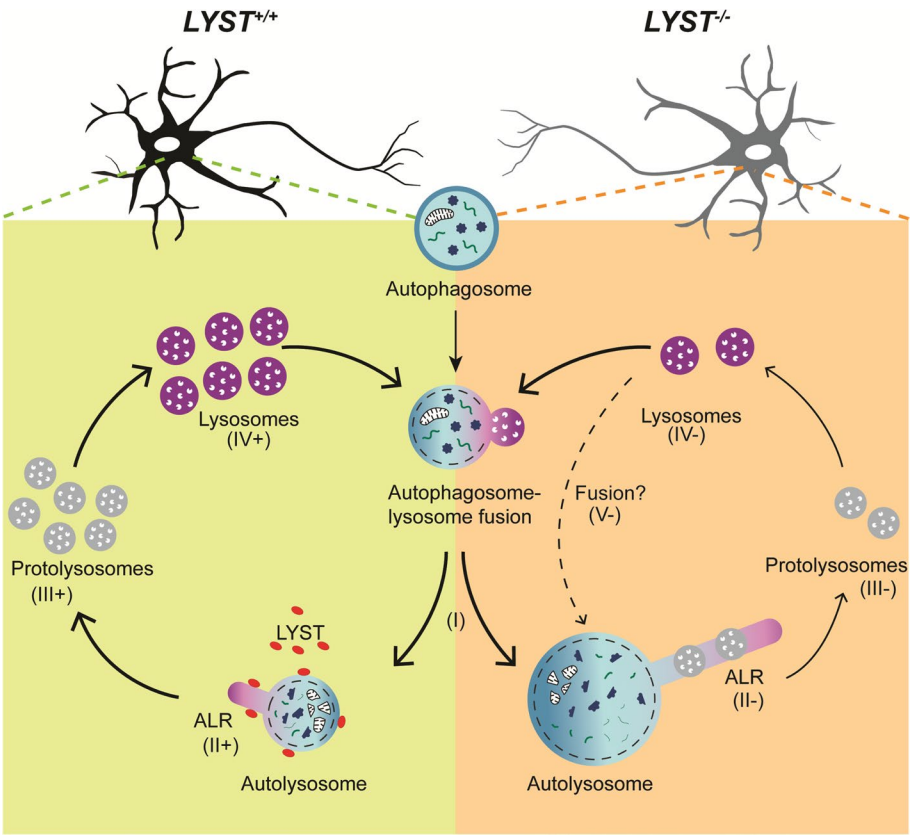

Fig. 6 Model illustrating the proposed role of LYST in regulating the autolysosome reformation fission step. During autophagy, the autophagosome-lysosome fuse to form the autolysosome, where the cargo degradation takes place (I). After cargo degradation, autolysosomes go through a recycling process name autolysosome reformation (ALR) to restore the number of the lysosomes consumed during autophagy (II). In wild-type neurons (II+), LYST (red spheres) may be recruited to the autolysosome membrane promoting the efficient tubule fission during ALR and therefore the re-formation of new protolysosomes (III+) that untimely mature into functional lysosomes (IV+). In LYST deficient neurons (II−), autolysosomes are bigger, tubules are hyperelongated, and the protolysosomes appear attached to the autolysosome tubule, likely due to impaired fission of autolysosome tubules. This led to fewer protolysosomes (III−) and eventually a depletion of functional lysosomes (IV−). Remaining free functional lysosomes may fuse with autolysosomes to respond the degradative needs of the cell (V−), at the same time increasing the autolysosome size in LYST deficient neurons

cell types opens new research avenues to further explore LYST function.

Materials and methods

Materials

Cell lines

WTC11 line: iPSC line derived from healthy human male adult skin fibroblasts (Coriell cell repository, Cat. No. GM25256).

i^3N iPSCs (Ngn2 iPSC) line: WTC11 line that harbors a single copy of doxycycline-inducible mouse *Ngn2* transgene at an adeno-associated virus integration site 1 (AAVS1) safe-harbor locus [17, 18]. i^3N iPSCs can be differentiated into a pure population of functional glutamatergic neurons (i^3Neurons) using the i^3Neuron differentiation protocol (see below).

CHS iPSC lines: iPSCs generated from the of CHD patients (generation and characterization as described previously [29]. The patient 1 genotype (CHS #1: c.1507C>T; p. Arg503*/c.9925G>A; p. Gly3309Ser) and patient 2 genotype (CHS #2: c.7951G>T; p.Val2651Phe/c.11039_11195del; p.Ala3680Glyfs*8).

Human osteosarcoma cell line (U2OS) (ATCC-HTB-96): Cells were authenticated by morphological assessment by microscopy and grown at 37 °C, 5% CO_2 using ATCC-formulated McCoy's 5a Medium Modified (Catalog No. 30-2007) supplemented with 10% fetal bovine serum (FBS).

All cell lines were tested routinely for mycoplasma contamination using the universal mycoplasma detection kit (ATCC, Cat. No. 30-1012K) following the manufacturer's instructions.

Plasmids

pLEX-PGK-LAMP1-mNeonGreen, pLEX-PGK-LAMP1-mApple, pLEX-PGK-EGFP-LC3, pLEX-PGK-Halo-LC3 were gifts from M. Ward (NINDS, NIH, USA); pTet-O-Ngn2-puro (Addgene; 52047); rtTA (Addgene; 20342); pSpCas9(BB)-2A-GFP (Addgene; PX458) the Lenti-X plasmids: pAdVantage, pMD2-G Coat protein and psPAX2 helper were obtained from Lofstrand Labs Ltd. To generate piggyBac (PB) transposon PB-LYST-ALFA hygro-NLS-mNeonGreen, the cDNA encoding full-length LYST was fused in frame with ALFA-tag and subcloned into PB-hygro-NLS-mNeonGreen (gift from M. Ward) backbone using NEBbuilder HiFi DNA Assembly cloning kit (New England BioLabs, Cat. No. E5520S). To generate pLEX-PGK-LAMP1-3xFLAG-APEX2, the cDNAs encoding full-length LAMP1, 3xFLAG and APEX2 were fused in-frame and subcloned into pLEX-PGK backbone using NEBbuilder HiFi DNA Assembly cloning kit.

Antibodies

Anti-cathepsin D antibody (IF: 1:200, WB: 1:500; R&D Systems, Cat. No. AF1014, AB_2087218); anti-LAMP1 (IF: 1:250; Hybridoma bank, Cat. No. H4A3, AB_2296838); Alexa Fluor 647 anti-ß-tubulin III (IF: 1:500; BioLegend, Clone TUJ1, AB_2315514); anti-ß-tubulin III (WB: 1:1000; STEMCELL technologies, Clone TUJ1, AB_2315514); anti-LC3 (WB: 1:1000; Sigma-Aldrich, Cat. No. L7543, AB_796155); anti-p62/SQSTM1 (WB: 1:1000; Sigma-Aldrich, Cat. No. P0067, AB_1841064); anti-vGlut1 (IF: 1:100; Millipore, Cat. No. MAB5502, AB_262185); anti-MAP2 (IF: 1:2000; Abcam, Cat. No. ab5392, AB_2138153); anti-FLAG (IF: 1:500, WB: 1:500; Sigma-Aldrich, Cat. No. F3165, AB_259529); anti-ALFA (IF: 1:250; WB: 1:500; NanoTag Biotechnologies, Clone 1G5); anti-Vinculin (WB: 1:5000; Sigma-Aldrich, Cat. No. V9131, AB_477629); anti-Actin (WB: 1:10,000; Sigma-Aldrich, Cat. No. A5316, AB_476743); Alexa Fluor 488 Streptavidin (IF: 1:500; Thermo Fisher Scientific, Cat. No. S11223); IRDye 680RD Streptavidin (WB: 1:1000; LI-COR, Cat. No. 926-68079).

Methods

Lentivirus production

Lentivirus were produced using Lenti-X™ 293T Cell Line (Takara, Cat. No. 632180). The day before the transfection, $1–1.5 \times 10^6$ cells/well were plated in a Poly-L-Ornithine (PLO; 0.1 mg/mL; Sigma-Aldrich, Cat. No. P3655)-coated six-well plate with 2 mL of DMEM complete media (Thermo Fisher Scientific) supplemented with 10% FBS and 1% pyruvate. To transfect the cells, 5 µL P3000™ Reagent (Lipofectamine^R 3000 Transfection Kit; Invitrogen, Cat. No. L3000-015) and 1.2 µg of lenti-packaging plasmids mix (0.8 µg psPAX2 helper, 0.3 µg pMD2-G Coat protein and 0.1 µg pAdVantage) was added to 150 µL of Opti-MEM I Reduced Serum Media (Gibco,Thermo Fisher Scientific, Cat. No. 31985-062) in an Eppendorf tube. In another Eppendorf tube 3.75 µL Lipofectamine^R 3000 Reagent (Lipofectamine^R 3000 Transfection Kit) was added to 150 µL of Opti-MEM I Reduced Serum. After incubation for 10 min, both tubes were mixed and further incubated at room temperature for 20 min. Following incubation, the transfection solution was gently added dropwise to each well, and the plate was gently moved to homogeneously mix with the 3 mL of fresh media. Twelve-14 h post-transfection, the media were replaced with fresh DMEM supplemented with ViralBoost™ Reagent (Alstem; Cat. No. VB100, diluted 1:500 in media). 46 h later, cell culture media was transferred to a 15 mL conical tube and centrifuged at room temperature for 10 min at 300*g* to pellet cell debris. Afterward, the supernatant was transferred into a new 15 mL conical tube and supplemented with Lenti-X™ Concentrator (Takara, Cat. No. 631231) in 3:1 ratio. Solutions were mixed by inversion and stored at 4 °C for 48 h. The viruses were pelleted by centrifugation at 4 °C for 30 min at 1500*g* and the supernatant was carefully removed. The virus-containing pellet was gently resuspended in PBS using 1/10th of the original volume. Aliquots of 50 µL of virus solution (required for infecting 1.5×10^6 iPSCs plated in one well of six-well plates) were stored at −80 °C.

Design and clone of single guide RNAs (sgRNAs)

The sgRNAs (targeting 5′ UTR and 3′UTR of the *LYST* gene*)* were designed using Benchling software (Benchling) to maximize on-target activity and minimize off-target effects. The sgRNA target sequences with cloning adapters were obtained from Integrated DNA Technologies (IDT) as single standard-desalted DNA oligos and cloned with BbsI into the plasmid pSpCas9(BB)-2A-GFP, bearing both sgRNA scaffold backbone (BB) and Cas9, pSpCas9.

Human iPSCs culture

All the iPSC lines were maintained under feeder-free conditions in a 37 °C, 5% CO_2 tissue culture incubator on Matrigel (BD Biosciences)-coated dishes. Cells were fed daily with fresh Essential 8 medium (Thermo Fisher Scientific). At 80–90% confluency, cells were washed with DPBS (Gibco, Thermo Fisher Scientific, Cat. No. 10010-023) and passaged either by Accutase (STEMCELL Technologies, Cat. No. 07920) at 37 °C for 5 min to enzymatically dissociate the iPSC colonies into single cells, or by 0.5 mM EDTA at room temperature for 5–7 min to

dissociate iPSCs into small clumps, for routine cell passaging. To promote cell survival during cell dissociation, the Essential 8 medium was supplemented with 10 µM of inhibitor of Rho-associated coiled-coil containing protein kinase (ROCK), Y-27632 (STEMCELL Technologies). Cells were frozen in 90% fetal bovine serum (EmbryoMax ES Cell Qualified FBS; Millipore, Cat. No. ES-009-B) and 10% DMSO (Sigma-Aldrich).

Generation of *LYST* knock out (*LYST*$^{-/-}$) iPSC line

i^{3}N iPSCs were dissociated with Accutase. 1×10^6 cells were seeded onto one well of a six-well Matrigel-coated plate in Essential 8 media supplemented with 10 µM Y-27632. The next day (16 h later) cells were co-transfected with 3 µg of two sgRNA plasmids (1.5 µg each), one targeted to the 3'UTR and the other 5′UTR region (sequence specified below) and 10 µL of Lipofectamine Stem transfection reagent (Thermo Fisher Scientific). After 48 h post-transfection, cells were dissociated by Accutase and the GFP positive cells were bulk sorted by a fluorescence-activated cell sorter (FACS) (BD Biosciences) and seeded in one Matrigel-coated well of a six-well dish. At 80–90% confluency, cells were dissociated using Accutase and single-cell sorted by FACS into Matrigel-coated 96-well plate. These cells were maintained in Essential 8 Flex medium (Thermo Fisher Scientific) supplemented with RevitaCell (Thermo Fisher Scientific, Cat. No. A2644501). After approximately 15 days (when the iPSC clone size occupies 3/4 of the well), clones were dissociated with 0.5 mM EDTA prepared in DPBS. For clonal expansion, 20% of the cells from each well were seeded in a new Matrigel-coated well of a 96-well dish for genotyping; and 80% were seeded into one Matrigel-coated well of a 12-well dish. After 2–3 days, genomic DNA was isolated from the cells growing in a 96-well dish using QuickExtract DNA (Lucigen, Cat. No. QE0905T), and genotyping was performed using PCR. The OUT-Fw primer (GAATGGAAGAGGCGGACGAT) and OUT-Rv Primer (TGTGTGTGGTGGGAGGAGTAT) were used to detect the KO and heterozygous alleles generated using the sgRNAs GAAGTTCATTCGCATTCACC and ACGCGT CACGCCTGCGACGC (combination A; KO [#32A] and the Heterozygous [#7A]). The OUT-Fw primer (GAATGG AAGAGGCGGACGAT) and OUT-Rv primer (TGAGCG GTTTGATCTTGGGA) were used to detect the KO and heterozygous alleles generated using the sgRNAs ATG AGCAGATCTCAAATCGA and ACGCGTCACGCCTGC GACGC (combination B; KO [#62B] and the Heterozygous [#63B]). The IN-Fw primer (CAGCCTAGGGGA GCAACAGA) and IN-Rv primer (CTTCTGAGTCATTGG CCGACT) that PCR amplify a region of the *LYST* exon seven were used to detect the WT alleles. Correctly edited clones were further expended and frozen as described above. The KO clone #32A (*LYST*$^{-/-}$) has been used for all experiments.

Karyotyping

To check the chromosomal integrity after the generation of the KO alleles, i^{3}PSC lines were treated with KaryoMAXTM ColcemidTM solution (10 µg/mL, Thermo Fisher scientific) to arrest the chromosomes at the metaphase stage of the cell cycle. Cells were then fixed in Carnoy's fixative (3:1, methanol: acetic acid) and cell spreads were made by dropping cell suspension onto the slides for DAPI banding analysis.

Differentiation of human iPSC-derived neurons

The differentiation protocol of iPSC (i^{3}N iPSC line) to i^{3}Neurons consists of a two-step protocol. (i) pre-differentiation and (ii) maturation. The protocol scheme is shown in Fig. 1a.

(i) Pre-differentiation of iPSC to i^{3}neuronal progenitor cells was carried out using the induction medium (IM), which consists of Dulbecco's modified Eagle's medium (DMEM)/F12, HEPES medium (Gibco, Thermo Fisher Scientific; Cat. No. 11330-057) containing N2 supplement (Gibco, Thermo Fisher Scientific; Cat. No. 17502-048), MEM Non-Essential Amino Acids (Gibco, Thermo Fisher Scientific; Cat. No. 11140-050), GlutaMAX (Gibco, Thermo Fisher Scientific; Cat. No. 35050-061), 10 nM ROCK inhibitor (Y-27632; STEMCELL Technologies) and 2 µg/mL doxycycline hydrochloride (Sigma-Aldrich; Cat. No. D9891). When iPSCs were 70–80% confluent, they were dissociated by Accutase from the plate, collected in conical tubes with DMEM/F12 medium (Gibco, Thermo Fisher Scientific, Cat. No. 11320-033) and centrifuged at 200*g* for 5 min. The pelleted cells were resuspended in IM, counted, and replated at density 1.5×10^6 cells/well in Matrigel-coated six-well plate with 2 mL of IM. The medium was changed daily for two additional days. ROCK inhibitor was added only for the first 24 h.

(ii) Maturation of i^{3}neuronal progenitor cells to i^{3}Neurons was carried out using cortical neuronal medium (CM), which consists of BrainPhys neuronal medium (STEMCELL Technologies, Cat. No. 05790) supplemented by B27 supplement (Gibco,Thermo Fisher Scientific, Cat. No. 17504-044), 50 ng/mL of brain-derived neurotrophic factor

(BDNF; PeproTech, Cat. No. 450-02), 50 ng/mL of neurotrophin-3 (NT-3; PeproTech; Cat. No. 450-03), 1 µg/mL Laminin mouse protein (Gibco, Thermo Fisher Scientific; Cat. No. 23017-015) and 2 µg/mL doxycycline hydrochloride. After three days of pre-differentiation, i^3neuronal progenitor cells were dissociated by Accutase and centrifuged at 200*g* for 5 min. Pelleted cells were resuspended in CM, counted, and replated at desired density in BioCoat PLO-coated plates or in µ-slide wells (Ibidi).

Generation of iNeurons by the introduction of lenti-*Ngn2*

iNeurons were generated following the protocol described by Zhang et al. [30] with some modifications. The protocol scheme is shown in Fig. 2h. On day-2, iPSCs (WT and CHS #1 and #2) were dissociated with Accutase and plated on Matrigel-coated six-well plate with Essential 8 medium and 10 µM ROCK inhibitor. The following day, (day-1), the medium was replaced with fresh Essential 8 medium and 50 µL of each virus (*Ngn2* and rtTA) was added to each well of a six-well plate. On day 0, the medium was replaced with fresh Essential 8 medium containing 2 µg/mL doxycycline, which was maintained in the medium throughout the differentiation protocol. From day 1 to day 4, the cells were growing with IM supplemented with 1.25 µg/mL of puromycin. On day 4, cells dissociated by Accutase and centrifuged at 200*g* for 5 min. Pelleted cells were resuspended in CM, counted, and replated at a desired density at BioCoat PLO-coated plates or µ-slide wells (Ibidi).

Generation of stable LYST-ALFA cell lines

For the generation of iPSC and U2OS cells stably overexpressing LYST-ALFA, cells grown in a well of six-well dish were co-transfected with the piggyBac transposon containing the coding sequence of LYST with in-frame C-terminus ALFA-tag (PB-LYST-ALFA hygro-NLS-mNeonGreen) together with piggyBac transposase plasmid (5:1) in a total of 3 µg of DNA and 10 µL of Lipofectamine Stem as a transfection reagent for the iPSC or Lipofectamine 3000 reagent for the U2OS cells. Cells were selected by the addition of hygromycin (200 µg/mL) 48 h post-transfection.

Labeling lysosomes with probes

For labeling active CathD, i^3Neurons were incubated with BODIPY-FL-pepstatin A (1 µM; Thermo Fisher Scientific, Cat. No. P12271) at 37 °C and 5% CO_2 for 1 h. The cells were imaged after washing twice with the neuronal media.

For labeling catalytic active Cath B, we used the Magic Red-Cathepsin B Assay (1:4000, ImmunoChemistry Technologies, Cat. No. 937) for 1 h at 37 °C and 5% CO_2. The cells were imaged after washing twice with the neuronal media.

For labeling acidic organelles, cells were incubated with 75 nM of LysoTracker Red DND-99 (Invitrogen, Cat. No. L7528) for 1 h at 37 °C and 5% CO_2. The cells were imaged after washing twice with the neuronal media.

For analyze the lysosomal protease activity, cells were incubated with DQ™ Red BSA (Invitrogen, Cat. No. D-12051) that becomes fluorescent upon proteolytic cleavage (λ_{ex}: ~ 590 nm, λ_{em}: ~ 620 nm). Cells were incubated with 10 µg/mL of DQ™ Red BSA for 1 h at 37 °C and 5% CO_2, followed by incubation with fresh media for 3 h.

Microfluidic assays

Microfluidic devices were fabricated using polydimethylsiloxane (PDMS). The design consists of two open chambers connected by microgrooves 5 µm wide, 4.5 µm high, and 450 µm, molded on photolithographically patterned templates designed and fabricated in-house. After un-molding and trimming of PDMS the devices were irreversibly bonded to acid-etched glass coverslips after activation with oxygen plasma. The coverslips were then coated with PLO. After 3 days of pre-differentiation, i^3neuronal progenitor cells were dissociated as described before, plated in one chamber of the microdevice, and cultured for at least 10 days to allow the axons to grow through the microgrooves to the other chamber for easy visualization.

Live cell imaging

For LAMP1-mNeonGreen trafficking experiments, we used Yakogawa CSU XI Spinning-disk with photometric Evolve Delta EMCCD on a Nikon Ti2e microscope. The objective and the environmental chamber were set at 37 °C with 5% CO_2 during the image acquisition. Spinning-disk images were taken in the mid-axon of $LYST^{+/+}$ and $LYST^{-/-}$ i^3Neurons (growing in microfluidic devices) with a Plan Apo VC 100X 1.35 NA silicone immersion oil objective. The movement of LAMP1-mNeonGreen positive vesicles was then imaged in 70 µm segments of the neuronal axons for 5 min. NIS-Elements AR Microscope imaging software was used for the acquisition. Kymographs were generated with Fiji software (Image J, NIH): lines of one-pixel thickness and 70 µm length were tracked through the axon and straightened, followed by stack re-slicing and Z projection. The number of retrograde, anterograde, or static events was determined manually from kymographs by looking at the slopes of the generated lines, with negative and positive slopes representing anterograde and retrograde movement, respectively. The results were expressed as a percentage of the total number of events in each kymograph.

Super-resolution live imaging was performed using Zeiss LSM 880 microscope equipped with a 63x/1.4 numerical aperture (NA) objective. Super-resolution imaging was performed using the Airyscan mode and the images were processed using Airyscan processing in ZEISS ZEN microscope software. The objective and the environmental chamber were set at 37 °C with 5% CO_2 during the image acquisition. Fiji software was used for image processing.

Immunofluorescence microscopy

Cells (iPSC, i^3Neurons or U2OS) were fixed for 10 min in 4% v/v PFA in PBS supplemented with 4% sucrose. Cells were then washed twice in PBS and permeabilized with permeabilization/blocking buffer: PBS containing 0.1% (w/v) saponin and 1% (w/v) BSA) for 1 h at room temperature. Fixed cells were incubated with primary antibodies diluted in permeabilization/blocking buffer overnight at 4 °C. The next day, after three five-min washes with permeabilization/blocking buffer, Alexa Fluor labeled secondary antibodies (Invitrogen) diluted 1:500 in permeabilization/blocking buffer were added for 1 h at room temperature. Nuclei were labeled with 5 µg/mL Hoechst 33342 (Sigma-Aldrich) in PBS and incubated at room temperature for 10 min. After three 5-min washes with PBS, slides were preserved using Ibid Mounting Medium (Cat. No. 50001). Cells were imaged using Zeiss LSM 700 microscope equipped with a 40X 1.2 NA and 63X 1.4 NA objective. Fiji software was used for image processing.

Immunoblotting

Cells were washed with PBS and lysed using 2X SDS lysis buffer (250 mM Tris–HCl pH 6.8, 4% SDS, 10% glycerol, Complete Protease Inhibitor Cocktail [Roche, Cat. No. 5892791001], and PhosSTOP phosphatase inhibitor cocktail [Roche, Cat. No. 4906845001]). Lysates were kept at room temperature, and sonicated at 10% amplitude with Branson Digital Sonicator for 30 s. Cleared lysates were obtained by centrifugation at 15,000*g* for 10 min and supernatants were transferred to new tubes. Protein concentrations were measured using the DC protein assay (Bio-Rad, Cat. No. 5000116). Twenty to 40 µg of total protein extracts were mixed with 2X SDS sample buffer containing 2-mercaptoethanol and resolved through SDS-PAGE on 4–15% Mini Protean TGX stain-Free Gels (Bio-Rad) and transferred to polyvinylidene fluoride (PVDF) or nitrocellulose membranes via a Trans-Blot Turbo Transfer System (BIO-RAD). Membranes were blocked in Odyssey blocking buffer (LI-COR, Cat. No. 927-60001) for 2 h at room temperature and probed with the primary antibodies overnight at 4 °C. Membranes were then washed with TBST (Tris-buffered saline with 0.05% Tween 20) followed by incubation with IRDye 680RD or IRDye 800CW labeled secondary antibodies (LI-COR Biosciences) for 1 h at room temperature. Images were captured on a LI-COR Odyssey CLx imaging system and analyzed using Image Studio software (LI-COR Biosciences).

APEX2 reaction

U2OS LYST-ALFA cells expressing LAMP1-3xFLAG-APEX2 were plated in a 10 cm^2 dish. When the cell density reached at 90%, media was replaced either with EBBS (Gibco, Cat. No. 24010-043) or basal media (growth media; GM), and cells were further incubated for 24 h. APEX2-mediated biotinylation reaction was carried out by supplementing cell media with 500 µM Biotinyl-tyramide (Biotin-phenol; Tocris, Cat. No. 6241) for 30 min at 37 °C and 5% CO_2 prior to APEX2 enzyme stimulation with the addition of hydrogen peroxide (H_2O_2) at room temperature. Cells were washed with 15 mL quencher solution (10 mM sodium azide, 10 mM sodium ascorbate, 5 mM Trolox in PBS) four times before lysing the cells with 500 µL of Lysis buffer (50 mM Tris–Cl pH 7.5, 500 mM NaCl, 0.2% SDS, 1 mM DTT, 10 mM sodium azide, 10 mM sodium ascorbate, 5 mM Trolox, complete mini protease inhibitor tablets in ddH_2O). Cells were then incubated on ice for 1 h and sonicated at 10% amplitude with Branson Digital Sonicator for 1 min on ice. Cleared lysates were obtained by centrifugation at 15,000*g* for 10 min at 4 °C and the protein concentration was quantified using a Pierce™ 660 nm Protein Assay (Thermo Fisher Scientific, Cat. No. 22660). Equal concentrations of protein lysates were incubated with pre-washed Streptavidin Magnetic Beads (Pierce, Cat. No. 88817) overnight with end-to-end rotation at 4 °C. The next day, using a magnetic rack, we washed twice the biotinylated proteins bound to streptavidin-conjugated beads with Buffer 1 (2% SDS in ddH_2O), twice with Buffer 2 (50 mM Tris–HCl pH 7.4, 500 mM NaCl, 0.1% sodium deoxycholate, 1% Triton-X, 1 mM EDTA in ddH_2O), twice with Buffer 3 (10 mM Tris–HCl pH 7.4, 250 mM NaCl, 0.5% sodium deoxycholate, 0.5% NP-40, 1 mM EDTA in ddH_2O), and twice with Buffer 4 (50 mM ammonium bicarbonate in ddH_2O). Biotinylated proteins were eluted from streptavidin-conjugated beads by boiling them at 95 °C for 5 min with 2X SDS sample buffer with 2-mercaptoethanol. The samples were then evaluated by immunoblotting.

Cell viability assay

LYST$^{+/+}$ and *LYST*$^{-/-}$ i^3Neurons were cultured in basal media (GM) or EBSS for 24 h. Cell viability was based on the cell's metabolic ability to reduce yellow tetrazolium salt (3-(4,5-dimethylthiazol-2-yl)-2,5-diphenyltetrazolium bromide or MTT; Roche, 11465007001) to purple formazan

crystals, which was measured fluorometrically following the manufacturer recommendation. The cell viability of *LYST*$^{+/+}$ and *LYST*$^{-/-}$ i^{3}Neurons was compared between GM and EBSS.

Quantification and statistical analysis

Multiple independent experiments were carried out as detailed in the figure legends. Quantified data were analyzed using Prism 9 software (Graphpad, San Diego, CA), and the statical significance of differences between two samples was calculated using a Mann–Whitney test. The Cath D signal was thresholded in Fiji software using the Otsu dark algorithm. After thresholding, images were made binary (run 'create a mask'), and a watershed function was run to separate objects that touch each other. Finally, the 'analyze particles' function (circularity set at 0.7–1.0) was used to quantify the number and size (area) of the Cath D signal (lysosome$_{CathD}$). The histograms were generated using the frequency distribution function from Prism 9 software. The bin width was set at 0.4. To generate histograms, the bin range was 0.2–1.8. To generate histograms shown in insets, the bin range was 1.8–4.6.

For the generation of line scan analysis, a straight line across the organelle was drawn as a Region of Interest (ROI) using Fiji software, and the values of intensity from each channel were determined. The related intensity profiles from the intensity values of each channel were generated using Prism 9 software.

Supplementary Information The online version contains supplementary material available at https://doi.org/10.1007/s00018-023-04695-x.

Acknowledgements The authors acknowledge National Human Genome Research Institute cytogenetics core for the iPSCs karyotyping; Stewart W. Humble (National Institute of Neurological Disorders and Stroke), Michael S. Fernandopulle (National Institute of Neurological Disorders and Stroke) and Jorge Gomez-Deza (*Eunice Kennedy Shriver* National Institute of Child Health and Human Development) for the technical advice. The authors also thank the Microfabrication and Microfluidics Unit of the Biomedical Engineering and Physical Science Shared Resource, National Institute of Biomedical Imaging and Bioengineering, for the assistance in the fabrication of the PDMS microdevices and templates; and Clàudia Serra Vinardell for her assistance in preparing graphic illustrations.

Author contributions JS-V, MBS, PS designing and conducting experiments, data analysis and interpretation, manuscript preparation-first draft, review, and editing. RDP helped with the trafficking experiments and data analysis. JM-L, JAB and AC contributed on microscopy data analysis. KK performed the bulk and single-cell sorting. WJI provided the CHS patients resources. MEW provided the i^{3}N iPSC line and plasmids. WAG funding acquisition, review, and editing. MCCM review and editing.

Funding This study is supported by the Intramural Research Programs of the National Human Genome Research Institute, National Institute of Child Health and Human Development, National Institute of Allergy and Infectious Diseases and National Heart, Lung, and Blood Institute of the National Institutes of Health.

Data availability All the relevant data are within the paper and its supporting Information. Numerical data are provided in the supplementary Excel file.

Declarations

Conflict of interest The authors have non-financial interests to disclose.

References

1. Yu L, McPhee CK, Zheng L, Mardones GA, Rong Y, Peng J, Mi N, Zhao Y, Liu Z, Wan F, Hailey DW et al (2010) Termination of autophagy and reformation of lysosomes regulated by mTOR. Nature 465:942–946. https://doi.org/10.1038/nature09076
2. Ferguson SM (2018) Axonal transport and maturation of lysosomes. Curr Opin Neurobiol 51:45–51. https://doi.org/10.1016/j.conb.2018.02.020
3. Lie PPY, Nixon RA (2019) Lysosome trafficking and signaling in health and neurodegenerative diseases. Neurobiol Dis 122:94–105. https://doi.org/10.1016/j.nbd.2018.05.015
4. Winckler B, Faundez V, Maday S, Cai Q, Guimas Almeida C, Zhang H (2018) The endolysosomal system and proteostasis: from development to degeneration. J Neurosci 38:9364–9374. https://doi.org/10.1523/JNEUROSCI.1665-18.2018
5. Sharma P, Nicoli E-R, Serra-Vinardell J, Morimoto M, Toro C, Malicdan MCV, Introne WJ (2019) Chediak-Higashi syndrome: a review of the past, present, and future. Drug Discov Today Dis Models 31:31–36
6. Kaplan J, De Domenico I, Ward DM (2008) Chediak-Higashi syndrome. Curr Opin Hematol 15:22–29. https://doi.org/10.1097/MOH.0b013e3282f2bcce
7. Introne W, Boissy RE, Gahl WA (1999) Clinical, molecular, and cell biological aspects of Chediak-Higashi syndrome. Mol Genet Metab 68:283–303. https://doi.org/10.1006/mgme.1999.2927
8. Barbosa MD, Nguyen QA, Tchernev VT, Ashley JA, Detter JC, Blaydes SM, Brandt SJ, Chotai D, Hodgman C, Solari RC, Lovett M et al (1996) Identification of the homologous beige and Chediak-Higashi syndrome genes. Nature 382:262–265. https://doi.org/10.1038/382262a0
9. Nagle DL, Karim MA, Woolf EA, Holmgren L, Bork P, Misumi DJ, McGrail SH, Dussault BJ Jr, Perou CM, Boissy RE, Duyk GM et al (1996) Identification and mutation analysis of the complete gene for Chediak-Higashi syndrome. Nat Genet 14:307–311. https://doi.org/10.1038/ng1196-307
10. Kypri E, Schmauch C, Maniak M, De Lozanne A (2007) The BEACH protein LvsB is localized on lysosomes and postlysosomes and limits their fusion with early endosomes. Traffic (Copenhagen, Denmark) 8:774–783. https://doi.org/10.1111/j.1600-0854.2007.00567.x
11. Perou CM, Leslie JD, Green W, Li L, Ward DM, Kaplan J (1997) The Beige/Chediak-Higashi syndrome gene encodes a widely expressed cytosolic protein. J Biol Chem 272:29790–29794. https://doi.org/10.1074/jbc.272.47.29790
12. Durchfort N, Verhoef S, Vaughn MB, Shrestha R, Adam D, Kaplan J, Ward DM (2012) The enlarged lysosomes in beige j cells result from decreased lysosome fission and not increased

lysosome fusion. Traffic 13:108–119. https://doi.org/10.1111/j.1600-0854.2011.01300.x
13. Sepulveda FE, Burgess A, Heiligenstein X, Goudin N, Menager MM, Romao M, Cote M, Mahlaoui N, Fischer A, Raposo G, Menasche G et al (2015) LYST controls the biogenesis of the endosomal compartment required for secretory lysosome function. Traffic 16:191–203. https://doi.org/10.1111/tra.12244
14. Rudelius M, Osanger A, Kohlmann S, Augustin M, Piontek G, Heinzmann U, Jennen G, Russ A, Matiasek K, Stumm G, Schlegel J (2006) A missense mutation in the WD40 domain of murine Lyst is linked to severe progressive Purkinje cell degeneration. Acta Neuropathol 112:267–276. https://doi.org/10.1007/s00401-006-0092-6
15. Hedberg-Buenz A, Dutca LM, Larson DR, Meyer KJ, Soukup DA, van der Heide CJ, Mercer HE, Wang K, Anderson MG (2019) Mouse models and strain-dependency of Chediak-Higashi syndrome-associated neurologic dysfunction. Sci Rep 9:6752. https://doi.org/10.1038/s41598-019-42159-0
16. Trantow CM, Hedberg-Buenz A, Iwashita S, Moore SA, Anderson MG (2010) Elevated oxidative membrane damage associated with genetic modifiers of Lyst-mutant phenotypes. PLoS Genet. 6:e1001008. https://doi.org/10.1371/journal.pgen.1001008
17. Wang C, Ward ME, Chen R, Liu K, Tracy TE, Chen X, Xie M, Sohn PD, Ludwig C, Meyer-Franke A, Karch CM et al (2017) Scalable production of iPSC-derived human neurons to identify tau-lowering compounds by high-content screening. Stem Cell Rep 9:1221–1233. https://doi.org/10.1016/j.stemcr.2017.08.019
18. Fernandopulle MS, Prestil R, Grunseich C, Wang C, Gan L, Ward ME (2018) Transcription factor-mediated differentiation of human iPSCs into neurons. Curr Protoc Cell Biol. 79:e51. https://doi.org/10.1002/cpcb.51
19. Perou CM, Kaplan J (1993) Chediak-Higashi syndrome is not due to a defect in microtubule-based lysosomal mobility. J Cell Sci 106(Pt 1):99–107. https://doi.org/10.1242/jcs.106.1.99
20. Wang C, Telpoukhovskaia MA, Bahr BA, Chen X, Gan L (2018) Endo-lysosomal dysfunction: a converging mechanism in neurodegenerative diseases. Curr Opin Neurobiol 48:52–58. https://doi.org/10.1016/j.conb.2017.09.005
21. Son JH, Shim JH, Kim KH, Ha JY, Han JY (2012) Neuronal autophagy and neurodegenerative diseases. Exp Mol Med 44:89–98. https://doi.org/10.3858/emm.2012.44.2.031
22. Yap CC, Digilio L, McMahon LP, Garcia ADR, Winckler B (2018) Degradation of dendritic cargos requires Rab7-dependent transport to somatic lysosomes. J Cell Biol 217:3141–159. https://doi.org/10.1083/jcb.201711039
23. Cheng XT, Xie YX, Zhou B, Huang N, Farfel-Becker T, Sheng ZH (2018) Characterization of LAMP1-labeled nondegradative lysosomal and endocytic compartments in neurons. J Cell Biol 217:3127–3139. https://doi.org/10.1083/jcb.201711083
24. Gil-Krzewska A, Saeed MB, Oszmiana A, Fischer ER, Lagrue K, Gahl WA, Introne WJ, Coligan JE, Davis DM, Krzewski K (2017) An actin cytoskeletal barrier inhibits lytic granule release from natural killer cells in patients with Chediak-Higashi syndrome. J Allergy Clin Immunol 142:914–27.e6. https://doi.org/10.1016/j.jaci.2017.10.040
25. Holland P, Torgersen ML, Sandvig K, Simonsen A (2014) LYST affects lysosome size and quantity, but not trafficking or degradation through autophagy or endocytosis. Traffic 15:1390–1405. https://doi.org/10.1111/tra.12227
26. Burkhardt JK, Wiebel FA, Hester S, Argon Y (1993) The giant organelles in beige and Chediak-Higashi fibroblasts are derived from late endosomes and mature lysosomes. J Exp Med 178:1845–1856. https://doi.org/10.1084/jem.178.6.1845
27. Lee JH, Yu WH, Kumar A, Lee S, Mohan PS, Peterhoff CM, Wolfe DM, Martinez-Vicente M, Massey AC, Sovak G, Uchiyama Y et al (2010) Lysosomal proteolysis and autophagy require presenilin 1 and are disrupted by Alzheimer-related PS1 mutations. Cell 141:1146–1158. https://doi.org/10.1016/j.cell.2010.05.008
28. Chen CS, Chen WN, Zhou M, Arttamangkul S, Haugland RP (2000) Probing the cathepsin D using a BODIPY FL-pepstatin A: applications in fluorescence polarization and microscopy. J Biochem Biophys Methods 42:137–151. https://doi.org/10.1016/s0165-022x(00)00048-8
29. Serra-Vinardell J, Sandler MB, Pak E, Zheng W, Dutra A, Introne W, Gahl WA, Christine Malicdan M (2020) Generation and characterization of four Chediak-Higashi Syndrome (CHS) induced pluripotent stem cell (iPSC) lines. Stem Cell Res. https://doi.org/10.1016/j.scr.2020.101883
30. Zhang Y, Pak C, Han Y, Ahlenius H, Zhang Z, Chanda S, Marro S, Patzke C, Acuna C, Covy J, Xu W et al (2013) Rapid single-step induction of functional neurons from human pluripotent stem cells. Neuron 78:785–798. https://doi.org/10.1016/j.neuron.2013.05.029
31. Li MA, Turner DJ, Ning Z, Yusa K, Liang Q, Eckert S, Rad L, Fitzgerald TW, Craig NL, Bradley A (2011) Mobilization of giant piggyBac transposons in the mouse genome. Nucleic Acids Res. 39:e148. https://doi.org/10.1093/nar/gkr764
32. Park MA, Jung HS, Slukvin I (2018) Genetic engineering of human pluripotent stem cells using PiggyBac transposon system. Curr Protoc Stem Cell Biol. 47:e63. https://doi.org/10.1002/cpsc.63
33. Woodard LE, Wilson MH (2015) PiggyBac-Ing models and new therapeutic strategies. Trends Biotechnol 33:525–533. https://doi.org/10.1016/j.tibtech.2015.06.009
34. Boland B, Kumar A, Lee S, Platt FM, Wegiel J, Yu WH, Nixon RA (2008) Autophagy induction and autophagosome clearance in neurons: relationship to autophagic pathology in Alzheimer's disease. J Neurosci 28:6926–6937. https://doi.org/10.1523/jneurosci.0800-08.2008
35. Min Y, Xu W, Liu D, Shen H, Xu Y, Zhang S, Zhang L, Wang H (2013) Earle's balanced salts solution and rapamycin differentially regulate the Bacillus Calmette-Guerin-induced maturation of human dendritic cells. Acta Biochim Biophys Sin (Shanghai) 45:162–169. https://doi.org/10.1093/abbs/gms117
36. Palmisano I, Della Chiara G, D'Ambrosio RL, Huichalaf C, Brambilla P, Corbetta S, Riba M, Piccirillo R, Valente S, Casari G, Mai A et al (2012) Amino acid starvation induces reactivation of silenced transgenes and latent HIV-1 provirus via down-regulation of histone deacetylase 4 (HDAC4). Proc Natl Acad Sci U S A 109:E2284–E2293. https://doi.org/10.1073/pnas.1202174109
37. Munson MJ, Allen GF, Toth R, Campbell DG, Lucocq JM, Ganley IG (2015) mTOR activates the VPS34-UVRAG complex to regulate autolysosomal tubulation and cell survival. EMBO J 34:2272–2290. https://doi.org/10.15252/embj.201590992
38. Lattao R, Rangone H, Llamazares S, Glover DM (2021) Mauve/LYST limits fusion of lysosome-related organelles and promotes centrosomal recruitment of microtubule nucleating proteins. Dev Cell 56:1000-1013.e6. https://doi.org/10.1016/j.devcel.2021.02.019
39. Hung V, Udeshi ND, Lam SS, Loh KH, Cox KJ, Pedram K, Carr SA, Ting AY (2016) Spatially resolved proteomic mapping in living cells with the engineered peroxidase APEX2. Nat Protoc 11:456–475. https://doi.org/10.1038/nprot.2016.018
40. Du W, Su QP, Chen Y, Zhu Y, Jiang D, Rong Y, Zhang S, Zhang Y, Ren H, Zhang C, Wang X et al (2016) Kinesin 1 drives autolysosome tubulation. Dev Cell 37:326–336. https://doi.org/10.1016/j.devcel.2016.04.014
41. Rong Y, McPhee CK, Deng S, Huang L, Chen L, Liu M, Tracy K, Baehrecke EH, Yu L, Lenardo MJ (2011) Spinster is required for autophagic lysosome reformation and mTOR reactivation

following starvation. Proc Natl Acad Sci 108:7826–7831. https://doi.org/10.1073/pnas.1013800108
42. Chang J, Lee S, Blackstone C (2014) Spastic paraplegia proteins spastizin and spatacsin mediate autophagic lysosome reformation. J Clin Investig 124:5249–5262. https://doi.org/10.1172/jci77598
43. Rong Y, Liu M, Ma L, Du W, Zhang H, Tian Y, Cao Z, Li Y, Ren H, Zhang C, Li L et al (2012) Clathrin and phosphatidylinositol-4,5-bisphosphate regulate autophagic lysosome reformation. Nat Cell Biol 14:924–934. https://doi.org/10.1038/ncb2557
44. Dai A, Yu L, Wang H-W (2019) WHAMM initiates autolysosome tubulation by promoting actin polymerization on autolysosomes. Nat Commun 10:3699. https://doi.org/10.1038/s41467-019-11694-9
45. McGrath MJ, Eramo MJ, Gurung R, Sriratana A, Gehrig SM, Lynch GS, Lourdes SR, Koentgen F, Feeney SJ, Lazarou M, McLean CA et al (2021) Defective lysosome reformation during autophagy causes skeletal muscle disease. J Clin Investig. https://doi.org/10.1172/jci135124
46. Schulze RJ, Weller SG, Schroeder B, Krueger EW, Chi S, Casey CA, McNiven MA (2013) Lipid droplet breakdown requires dynamin 2 for vesiculation of autolysosomal tubules in hepatocytes. J Cell Biol 203:315–326. https://doi.org/10.1083/jcb.201306140
47. Maday S, Holzbaur EL (2016) Compartment-specific regulation of autophagy in primary neurons. J Neurosci 36:5933–5945. https://doi.org/10.1523/jneurosci.4401-15.2016
48. Mizushima N, Yamamoto A, Matsui M, Yoshimori T, Ohsumi Y (2004) In vivo analysis of autophagy in response to nutrient starvation using transgenic mice expressing a fluorescent autophagosome marker. Mol Biol Cell 15:1101–1111. https://doi.org/10.1091/mbc.e03-09-0704
49. Mizushima N, Komatsu M (2011) Autophagy: renovation of cells and tissues. Cell 147:728–741. https://doi.org/10.1016/j.cell.2011.10.026
50. Varga RE, Khundadze M, Damme M, Nietzsche S, Hoffmann B, Stauber T, Koch N, Hennings JC, Franzka P, Huebner AK, Kessels MM et al (2015) In vivo evidence for lysosome depletion and impaired autophagic clearance in hereditary spastic paraplegia type SPG11. PLoS Genet 11:e1005454. https://doi.org/10.1371/journal.pgen.1005454
51. Boutry M, Branchu J, Lustremant C, Pujol C, Pernelle J, Matusiak R, Seyer A, Poirel M, Chu-Van E, Pierga A, Dobrenis K et al (2018) Inhibition of lysosome membrane recycling causes accumulation of gangliosides that contribute to neurodegeneration. Cell Rep 23:3813–3826. https://doi.org/10.1016/j.celrep.2018.05.098
52. Khundadze M, Ribaudo F, Hussain A, Stahlberg H, Brocke-Ahmadinejad N, Franzka P, Varga R-E, Zarkovic M, Pungsrinont T, Kokal M, Ganley IG et al (2021) Mouse models for hereditary spastic paraplegia uncover a role of PI4K2A in autophagic lysosome reformation. Autophagy 17:3690–3706. https://doi.org/10.1080/15548627.2021.1891848
53. Dehay B, Bové J, Rodríguez-Muela N, Perier C, Recasens A, Boya P, Vila M (2010) Pathogenic lysosomal depletion in Parkinson's disease. J Neurosci 30:12535–12544. https://doi.org/10.1523/jneurosci.1920-10.2010
54. Magalhaes J, Gegg ME, Migdalska-Richards A, Doherty MK, Whitfield PD, Schapira AHV (2016) Autophagic lysosome reformation dysfunction in glucocerebrosidase deficient cells: relevance to Parkinson disease. Hum Mol Genet 25:3432–3445. https://doi.org/10.1093/hmg/ddw185
55. Komatsu M, Waguri S, Chiba T, Murata S, Iwata J-i, Tanida I, Ueno T, Koike M, Uchiyama Y, Kominami E, Tanaka K (2006) Loss of autophagy in the central nervous system causes neurodegeneration in mice. Nature 441:880–884. https://doi.org/10.1038/nature04723
56. Marks MS, Heijnen HF, Raposo G (2013) Lysosome-related organelles: unusual compartments become mainstream. Curr Opin Cell Biol 25:495–505. https://doi.org/10.1016/j.ceb.2013.04.008
57. Ripoll L, Heiligenstein X, Hurbain I, Domingues L, Figon F, Petersen KJ, Dennis MK, Houdusse A, Marks MS, Raposo G, Delevoye C (2018) Myosin VI and branched actin filaments mediate membrane constriction and fission of melanosomal tubule carriers. J Cell Biol 217:2709–2726. https://doi.org/10.1083/jcb.201709055